

Carbon Capture via Crystallization with a Guanidine Ligand



Approved for public release. Distribution is unlimited.

Radu Custelcean
Costas Tsouris

Oak Ridge National
Laboratory
Oak Ridge, TN 37831

Jorge Gabitto (subcontract)

Prairie View A&M
University
Prairie View, TX 77446

January 31, 2019

DOCUMENT AVAILABILITY

Reports produced after January 1, 1996, are generally available free via US Department of Energy (DOE) SciTech Connect.

Website <http://www.osti.gov/scitech/>

Reports produced before January 1, 1996, may be purchased by members of the public from the following source:

National Technical Information Service
5285 Port Royal Road
Springfield, VA 22161
Telephone 703-605-6000 (1-800-553-6847)
TDD 703-487-4639
Fax 703-605-6900
E-mail info@ntis.gov
Website <http://www.ntis.gov/help/ordermethods.aspx>

Reports are available to DOE employees, DOE contractors, Energy Technology Data Exchange representatives, and International Nuclear Information System representatives from the following source:

Office of Scientific and Technical Information
PO Box 62
Oak Ridge, TN 37831
Telephone 865-576-8401
Fax 865-576-5728
E-mail reports@osti.gov
Website <http://www.osti.gov/contact.html>

This report was prepared as an account of work sponsored by an agency of the United States Government. Neither the United States Government nor any agency thereof, nor any of their employees, makes any warranty, express or implied, or assumes any legal liability or responsibility for the accuracy, completeness, or usefulness of any information, apparatus, product, or process disclosed, or represents that its use would not infringe privately owned rights. Reference herein to any specific commercial product, process, or service by trade name, trademark, manufacturer, or otherwise, does not necessarily constitute or imply its endorsement, recommendation, or favoring by the United States Government or any agency thereof. The views and opinions of authors expressed herein do not necessarily state or reflect those of the United States Government or any agency thereof.

Approved for public release. Distribution is unlimited.

Carbon Capture via Crystallization with a Guanidine Ligand

SUBMITTED BY

Radu Custelcean and Costas Tsouris
Oak Ridge National Laboratory
1 Bethel Valley Road
Oak Ridge, TN 37930

PRINCIPAL INVESTIGATOR

Radu Custelcean, Ph.D.
(865) 574-5018
custelceanr@ornl.gov

Prepared by
OAK RIDGE NATIONAL LABORATORY
Oak Ridge, TN 37831-6283
managed by
UT-BATTELLE, LLC
for the
US DEPARTMENT OF ENERGY
under contract DE-AC05-00OR22725

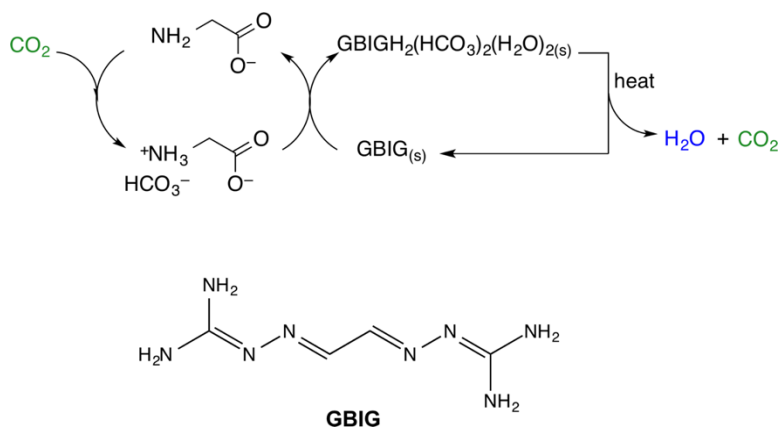
January 31, 2019

CONTENTS

1. SUMMARY	1
2. BACKGROUND INFORMATION	2
3. EXPERIMENTAL RESULTS AND DISCUSSION	3
3.1 General Approach	3
3.2 Sorbent Selection and Testing	3
3.3 Stirred Tank Bubble Reactor Loading	6
3.4 Bubble Column Reactor Loading	7
3.5 Sorbent Regeneration by Guanidine Crystallization	13
3.6 CO ₂ Separation Cycles	15
4. MODELING RESULTS AND DISCUSSION	17
4.1 Two-Phase Batch Reactor Modeling	20
4.2 Bubble Column Modeling	23
4.3 Modeling Discussion	24
5. TECHNO-ECONOMIC ANALYSIS	30
5.1 MEA Benchmark Calculations	31
5.2 Amino Acid/Guanidine System Calculations	33
5.3 Economic Calculations	35
6. CONCLUSIONS	37
7. REFERENCES	38
8. PRODUCTS	41
8.1 Publications and presentations	41
8.2 Technology commercialization	41
9. APPENDIX	42

1. SUMMARY

A hybrid solvent/solid-state approach to CO₂ separation from flue gas is demonstrated based on absorption with aqueous amino acids (i.e., glycine, sarcosine), followed by crystallization of the bicarbonate salt of glyoxal-bis(iminoguanidine) (GBIG), and subsequent solid-state CO₂ release from the bicarbonate crystals. In this process, GBIG bicarbonate crystallization regenerates the amino acid sorbent, and the CO₂ is subsequently released by mild heating of the GBIG bicarbonate crystals, which results in quantitative, energy-efficient regeneration of GBIG. The cyclic capacities measured from multiple absorption-regeneration cycles are in the range of 0.2-0.3 mol CO₂/mol amino acid. This hybrid CO₂ separation approach reduces the sorbent regeneration energy by 24% and 40% compared to benchmark industrial sorbents monoethanolamine (MEA) and sodium glycinate (SG), respectively, while minimizing the amount of the amino acid sorbent loss through evaporation or degradation.



The glycine and sarcosine sorbents were tested for CO₂ absorption using a stirred bubble tank reactor and a bubble column reactor. The experimental information thus obtained was used to develop a mathematical model for the prediction of the CO₂ absorption performance under a wide range of operating conditions. Finally, the experimental and modelling data were used in a techno-economic analysis to evaluate the economic feasibility of this new CO₂ capture technology and compare it with the MEA benchmark. The analysis found a 10% reduction in the cost of CO₂ avoided compared to MEA.

Acknowledgement. Funding for this research was provided by the the U.S. Department of Energy, Office of Technology Transitions, through a Technology Commercialization Fund (TCF-17-13299).

2. BACKGROUND INFORMATION

Carbon capture and storage (CCS) is an important strategy aimed at stabilizing the atmospheric CO₂ concentration and thereby the global temperature. In conventional fossil fuel-fired power plants, the resulting flue gas is released into the air without any carbon dioxide scrubbing, which gradually increases the atmospheric CO₂ concentration (currently at approximately 409 ppm). Implementation of post-combustion capture (PCC) of carbon dioxide, whereby the CO₂ emitted by power plants is captured and stored into geological repositories, would enable us to continue to use relatively cheap fossil fuels such as coal, natural gas, and oil, but with significantly reduced CO₂ emissions. A recent report by the International Energy Agency indicated that by 2050 CCS could reduce the annual CO₂ emissions by almost 6 gigatonnes, which represents about 14% of the total carbon emission reduction necessary to limit the global temperature increase by 2 °C by the end of the 21st century (International Energy Agency, 2016). This goal will be accomplished by developing inexpensive materials that can be used to effectively capture CO₂ and be regenerated with minimal energy penalty. This project helped address this need by introducing new materials and mechanisms for CO₂ capture.

The most established PCC technology is based on amine scrubbing, a process in which an aqueous amine sorbent is contacted with the flue gas in an absorption column, resulting in the chemical reaction of CO₂ with the amine to form carbamate and bicarbonate species (Feron, 2016). The CO₂-rich amine is then transferred to a stripping column, where it is steam-heated to 100-140 °C to release the CO₂ and regenerate the amine absorbent. One major advantage of this technology is that it can be easily retrofitted into existing coal- or natural gas-burning power plants. Alternative PCC technologies based on solid sorbents, ionic liquids, or membranes have been considered, but to date they have not been able to disrupt the aqueous amine scrubbing technology, which remains the method of choice in PCC due to the high selectivity for CO₂ and the high rate of absorption. Currently, the benchmark amine scrubbing technology is based on 30 wt% (~5M) aqueous monoethanolamine (MEA), which costs about \$50-60/metric ton CO₂. For any new sorbent to be able to replace MEA it would have to surpass it in several key performance criteria including energy consumption, capital and operational costs, environmental impact, and robustness and resistance to degradation. MEA has several limitations. It has high regeneration energy (due to the high heat capacity of the aqueous solution and the substantial water vaporization during stripping); it has relatively low cyclic capacity; it is volatile and susceptible to thermal and chemical degradation, resulting in significant sorbent loss over time; it reacts irreversibly with flue gas components such as SO_x and NO_x, requiring complete removal of these gases prior to CO₂ scrubbing; it is corrosive and toxic to the environment. These significant drawbacks prompted the search for a superior sorbent, which so far has met with limited success as improvements on one front often lead to decreased performance in other criteria. For instance, aqueous potassium carbonate has higher capacity and lower regeneration energy, is cheaper, more stable, less corrosive and toxic, and more resistant to degradation compared to most amines; its rate of CO₂ absorption, however, is much lower compared to that of MEA. One possible solution is to employ mixed sorbents that combine for example the high absorption rate of primary and secondary amines with the higher capacity of tertiary amines or potassium carbonate. However, most innovations in PCC to date have been incremental in nature and failed to provide a ‘game changer’ alternative to the amine scrubbing technology (Feron, 2016).

The goal of this project was to demonstrate a bench-scale CO₂ capture process based on a novel guanidinium (bi)carbonate crystallization approach, and ultimately develop an energy-efficient and cost-effective technology for CO₂ capture from flue gas. The project built on our recent

discovery of a new class of aqueous guanidine sorbents that react with carbon dioxide and crystallize as carbonate or bicarbonate salts of very low aqueous solubility (Brethomé, 2018; Williams, 2019). The resulting guanidinium (bi)carbonate crystals release the CO₂ upon mild heating at 80-120 °C, which regenerates the guanidine ligands quantitatively (Figure 1). The potential advantage of this crystallization-based approach over traditional amine scrubbing methods (i.e., using aqueous MEA) is that it allows sorbent regeneration by heating the solid crystals alone, without the bulk solution, making this process more energy-efficient.

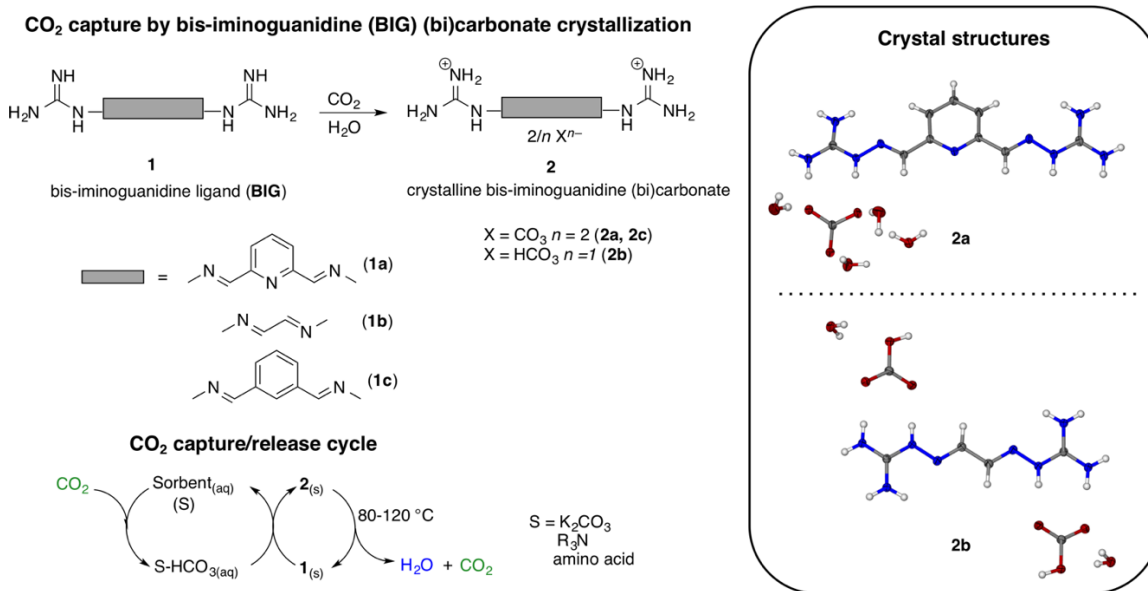


Figure 1. CO₂ capture by crystallization with guanidine ligands (**1**) as (bi)carbonate salts (**2**).

3. EXPERIMENTAL RESULTS AND DISCUSSION

3.1 General Approach

The project had three technical objectives: identification of an optimal absorbent with favorable kinetics and thermodynamics (Task 1); optimization of guanidinium bi(carbonate) crystallization and CO₂ stripping (Task 2); and economic evaluation of the proposed technology and comparison with current carbon capture technologies (Task 3). The three tasks were approached by a combined experimental and theoretical methodology. First, a series of sorbents were tested for their CO₂ capacity and absorption rate, as well as compatibility for crystallization with guanidinium (bi)carbonate. The top two sorbents were selected for further CO₂ absorption tests using a stirred bubble tank reactor and a bubble column reactor. The experimental information thus obtained was used to develop a mathematical model for the prediction of the CO₂ absorption performance under a wide range of operating conditions. Finally, the experimental and modelling data were used in a techno-economic analysis to evaluate the economic feasibility of the CO₂ capture technology.

3.2 Sorbent Selection and Testing

The objective of this task was to identify an optimal sorbent with fast CO₂ absorption rate, high capacity, good resistance to degradation, and compatibility for crystallization with the guanidinium (bi)carbonate. We initially tested potassium carbonate (K₂CO₃) and triethanolamine (TEA) for

CO₂ sorption with a flue gas simulant (13% CO₂ + 87% N₂) on a small-scale (20 mL) using a fritted bubbler (Figure 2).

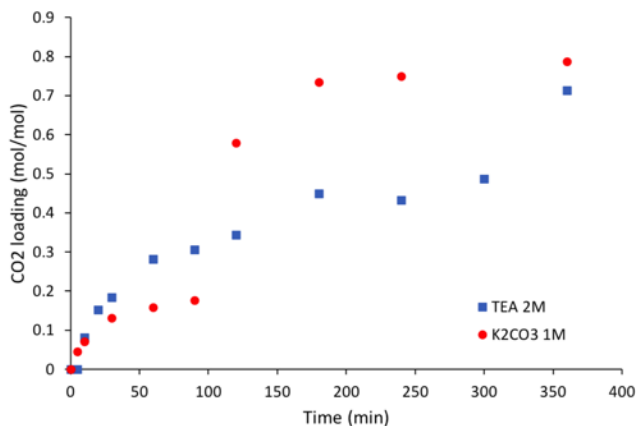
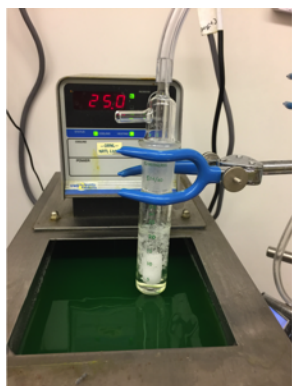


Figure 2. CO₂ absorption curves for aqueous TEA (2 M) and aqueous K₂CO₃ (1 M). A flue gas simulant (12.8% CO₂ + 87.2% N₂) was bubbled through solutions at a rate of 0.4 L/min using a fritted bubbler (shown on the left).

As the K₂CO₃ and TEA sorbents showed rates of CO₂ absorption that were too slow for practical CO₂ separation (≈3 hrs to reach saturation), we tested the effect of different rate promoters such as glycine and sarcosine amino acids in combination with K₂CO₃, or carbonic anhydrase (CA) in combination with TEA. The carbonic anhydrase enzyme did not show any rate increase compared to uncatalyzed TEA (Figure 3), which could be due to the inactivation of the enzyme in the caustic TEA sorbent (pH = 11.1).

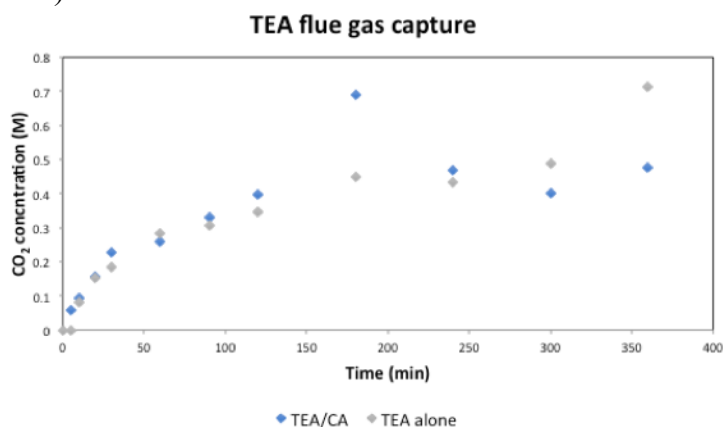


Figure 3. CO₂ absorption with aqueous TEA (2 M) with (blue) or without CA catalyst (grey).

The glycine and sarcosine amino acids (Shariff, 2016), on the other hand, significantly enhanced the rate of the CO₂ absorption with the K₂CO₃ sorbent (0.9 M carbonate + 0.1 M amino acid), which now reached saturation in about 40 min. However, the pure amino acid sorbents (1 M glycine or sarcosine, as potassium salts) showed by far the best performance, reaching maximum loading capacity of about 1 mol CO₂ per mol of amino acid in just 20 min (Figure 4). The observed rates of absorption for the amino acid sorbents were significantly higher than those observed for the MEA benchmark, which took about 2 hours to fully load under these conditions. The glycine

and sarcosine amino acids were therefore selected as the sorbents of choice for further testing and optimization. The glycine sorbent was also tested at higher concentration (2 M) and showed no decrease in performance, reaching a maximum loading of 2 M CO₂, as a mixture of 74% bicarbonate and 26% carbamate (Figure 5).

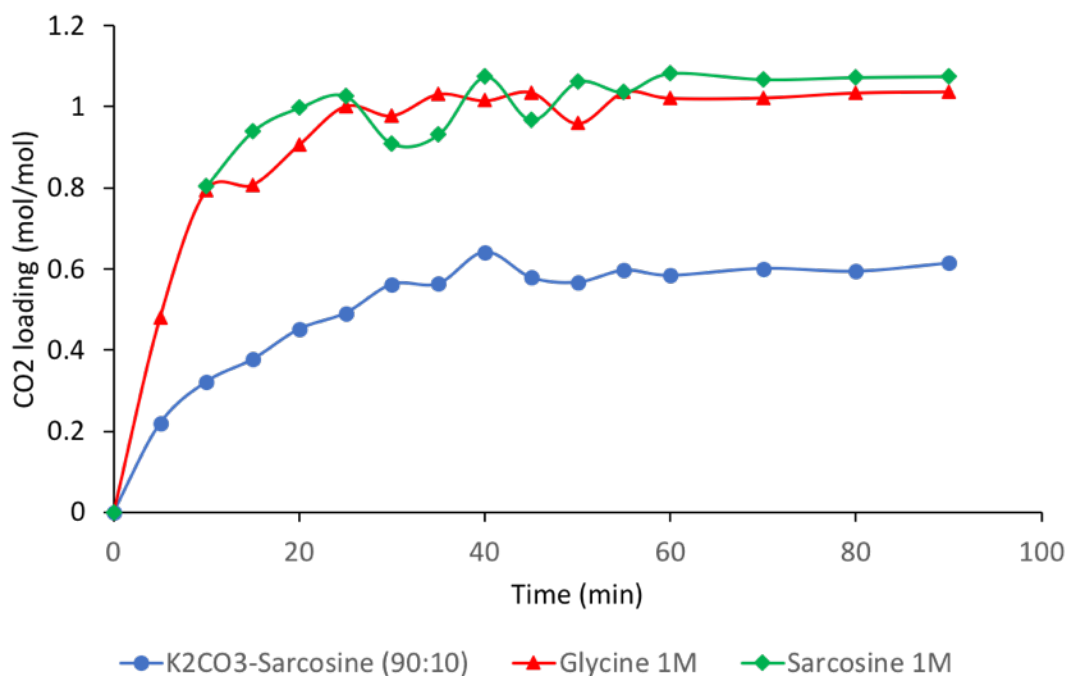


Figure 4. CO₂ absorption curves for amino acid-promoted K₂CO₃ sorbent (0.9 M carbonate + 0.1 M amino acid), compared to pure amino acid sorbents (1 M glycine or sarcosine as potassium salts). The flue gas simulant (12.8% CO₂ + 87.2% N₂) was bubbled through a 20 mL sorbent solution using a fritted bubbler, at a flow rate of 0.4 L/min.

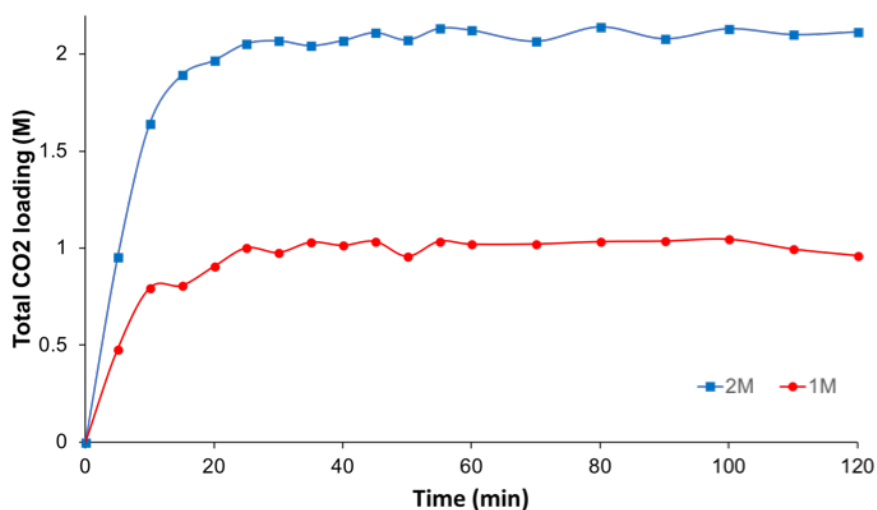


Figure 5. CO₂ absorption curves for 1 M vs. 2 M glycine sorbents.

3.3 Stirred Tank Bubble Reactor Loading

Having established the glycine and sarcosine amino acids as the optimal sorbents for CO₂ scrubbing from flue gas, we next proceeded with scaling up the reaction and optimizing the CO₂ loading. For this purpose, we used a 1 L VirTis Omni-Culture stirred tank reactor consisting of a 1.6 L flask, an impeller for stirring, and a heat exchanger with baffles. A porous Teflon tube (10 μm pore diameter) was attached along the impeller support on the bottom of the reactor to generate the bubbles. The temperature of the reactor was set at 25 ± 1 °C using a chiller with circulating coolant. A 1 L aqueous solution of 1 M potassium hydroxide and 1 M glycine/sarcosine was added to the reactor. The stirrer was set to 450 rpm, and the flue gas flow rate was set at 4 L/min. The pH probe was placed inside the reactor to record the evolution of the solution pH *in situ*. A temperature probe was also located inside the reactor to monitor the temperature of the reaction. The loading experiments were run for a duration of 2 hours, with samples taken every 5 minutes for the first hour, and every 10 minutes for the remaining hour. The concentrations of carbonate and carbamate formed were determined by ion chromatography (IC) and proton nuclear magnetic resonance (¹H NMR) spectroscopy, respectively. The results are summarized in Table 1, and the CO₂ loading curves are shown in Figure 6.

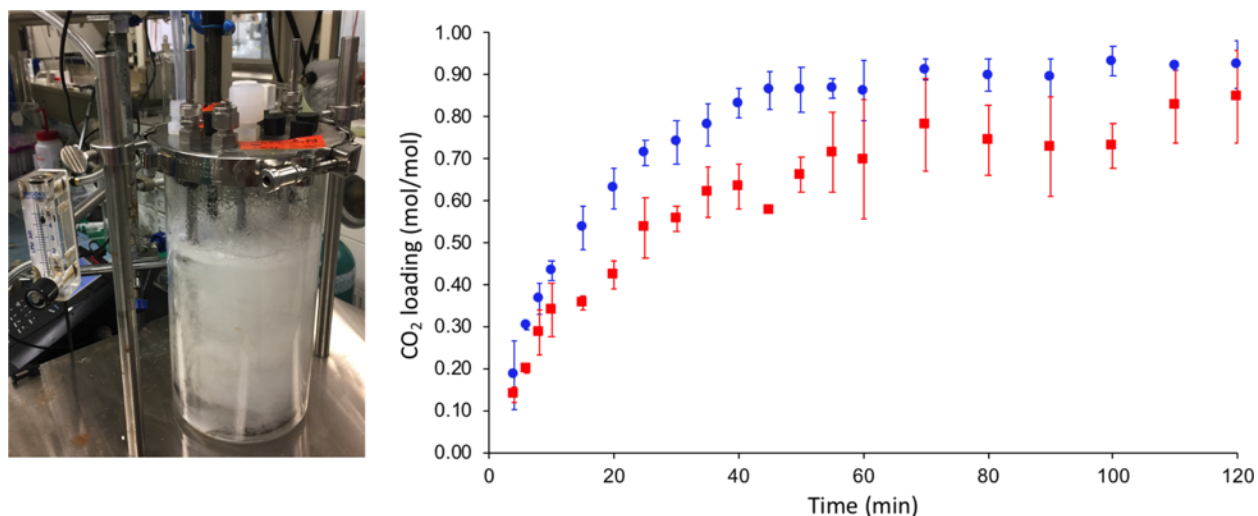


Figure 6. CO₂-loading curves for a flue gas simulant (12.8% CO₂) with 1 M potassium glycinate (blue dots) or potassium sarcosinate (red squares) sorbents, using a bubble reactor (shown on the left). The CO₂ loading values correspond to the sums of the (bi)carbonate and carbamate concentrations in solution, relative to the molar concentrations of the amino acids. The error bars are defined as the standard deviations from three separate absorption experiments.

Table 1. Equilibrium loading values for CO₂ capture with 1 M aqueous solutions of potassium glycinate or sarcosinate at 25 °C. Three different absorption experiments were done for each amino acid, and the reported concentrations are the average values for the three runs after 2 hrs.

Sorbent	pH (initial/final)	Carbonate ^a (M)	Carbamate (M)	Total CO ₂ (M)
Glycine (1M)	12.2/8.2	0.81 ± 0.07	0.11 ± 0.01	0.92 ± 0.06
Sarcosine (1M)	12.4/8.4	0.78 ± 0.11	0.07 ± 0.01	0.85 ± 0.11

^a As the sum of CO₃²⁻ and HCO₃⁻ concentrations.

The equilibrium CO₂ loading capacities measured for glycine and sarcosine are 0.92 ± 0.06 and 0.85 ± 0.11 mol/mol, with most CO₂ absorbed as (bi)carbonate, and to a lesser extent as carbamate. The CO₂ breakthroughs were observed after about 20 min for both the glycine and sarcosine sorbents (Figure 7).

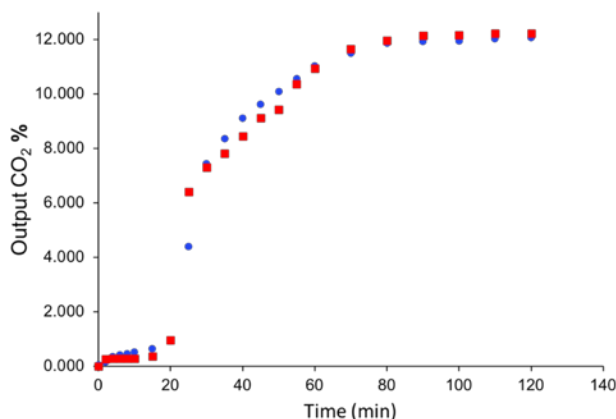


Figure 7. CO₂ breakthrough curves for glycine (blue dots) and sarcosine (red square) sorbents.

3.4 Bubble Column Reactor Loading

The goal of these experiments was to study CO₂ absorption using amino acid salts in a gas-liquid bubble column reactor (BCR) where the liquid phase is recirculated to concentrate the amount of the products of the CO₂ absorption. BCR was identified as a suitable reactor for carbon capture due the following potential advantages: (i) BCRs have high heat and mass transfer performance, (ii) a bubble diffuser placed at the bottom of the column helps disperse the gas phase so that mechanical mixing is not required, (iii) BCRs are very easy to operate since there have no moving parts, thus making it easy to add or withdraw liquid from the system.

A 3 L bubble column reactor with a bubble diffuser located at the bottom of the column and with the liquid phase operating in recycle mode was used to carry out the loading experiments. Two different alkaline amino acid solutions of 1 M sarcosine and glycine, at pH~12, and a flue gas mixture containing 13% CO₂ with a gas flowrate of 4.4 Lmin⁻¹ were used in these experiments. A process flow diagram of the setup used in the study can be seen in Figure 8. As part of this study, all the important parameters characterizing the reactor operation, e.g., bubble size distribution, liquid phase dispersion coefficient, and gas hold-up, were experimentally determined.

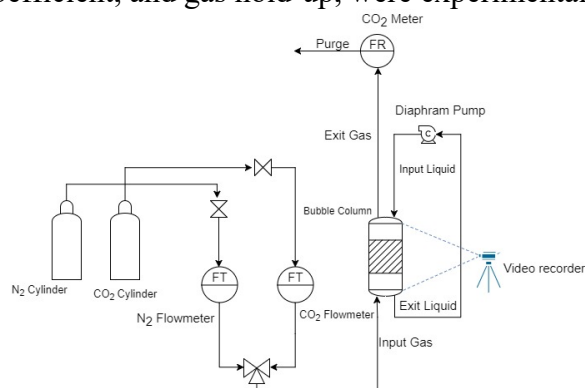


Figure 8. Experimental setup used for CO₂ absorption from simulated flue gas. The solvent was continuously recycled and pumped through the bubble column with the help of a diaphragm pump. CO₂ and N₂ were drawn from individual cylinders and mixed at predetermined flowrates to simulate flue gas concentrations.

Exit pH and Gas Concentration Profiles. As CO₂ absorption reactions proceed, the solution becomes less basic. Figures 9A and 9B illustrate the change in pH over the reaction time, which drops from 11-12 to about 8. Figures 9C and 9D display the exit CO₂ profile for glycine/KOH and sarcosine/KOH, respectively. From these figures it can be seen that the CO₂ breakthrough with the glycine and sarcosine solutions occurred at around 53 min and 57 min, respectively. Figure 9C also illustrates the effect of increasing the flowrate of CO₂ to 1240 mL min⁻¹ (while keeping the N₂ flowrate constant) on the exit CO₂ concentration profile, which shortened the breakthrough time to about 30 minutes. This is because the glycine sorbent becomes saturated faster when a higher inlet flowrate of CO₂ is used.

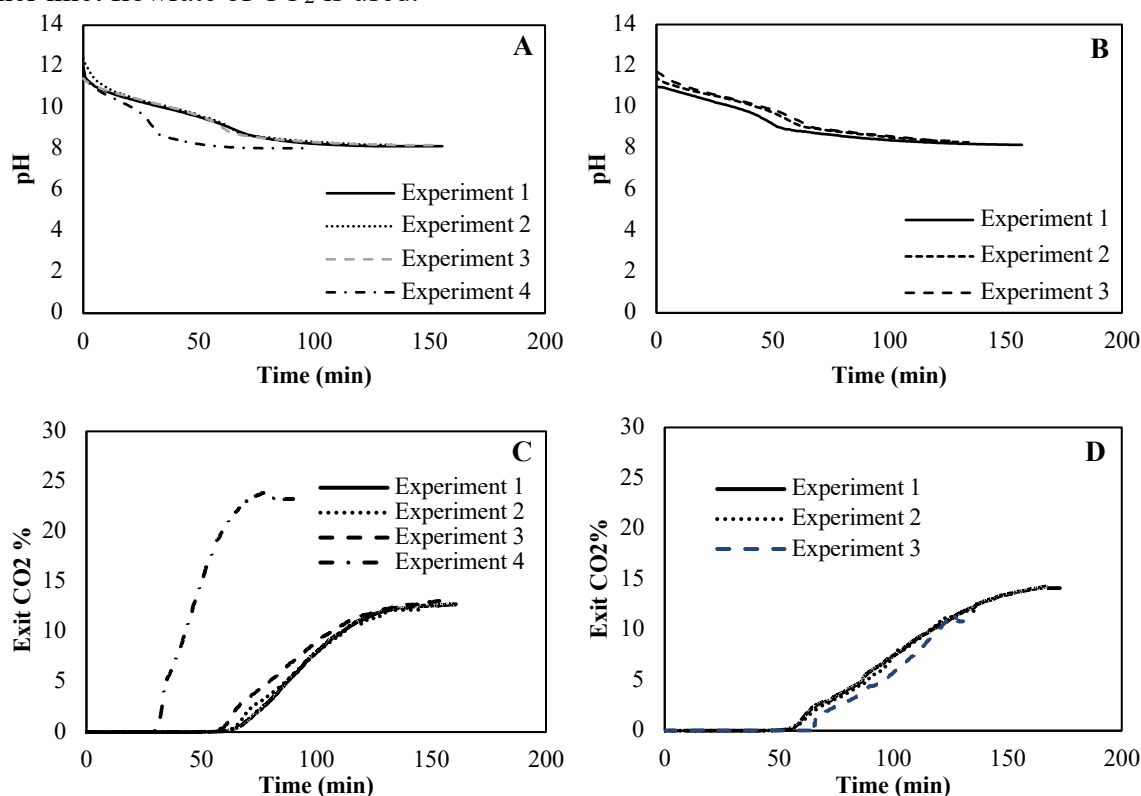


Figure 9. Exit pH and CO₂ concentration profiles: (A) Exit pH profile for glycine/KOH; (B) Exit pH profile for sarcosine/KOH; (C) Exit gas CO₂ concentration profile for glycine/KOH; (D) Exit gas CO₂ concentration profile for sarcosine/KOH.

Gas Hold-Up. Figure 10 illustrates the effect of time on the gas-phase holdup in glycine/KOH (A) and sarcosine/KOH (B) solutions. In all cases, the gas-phase holdup is seen to increase over the course of the reaction. This is because as time increases, the uptake rate of gaseous CO₂ decreases, thus the volume of the gas phase increases with time. In glycine promoted solutions, the average initial gas-phase holdup is 10.4% and the average final gas phase holdup is 14.4%. Similarly, in sarcosine promoted solutions, the average initial gas-phase holdup is 6.0% and the average final gas phase holdup is 8.5%.

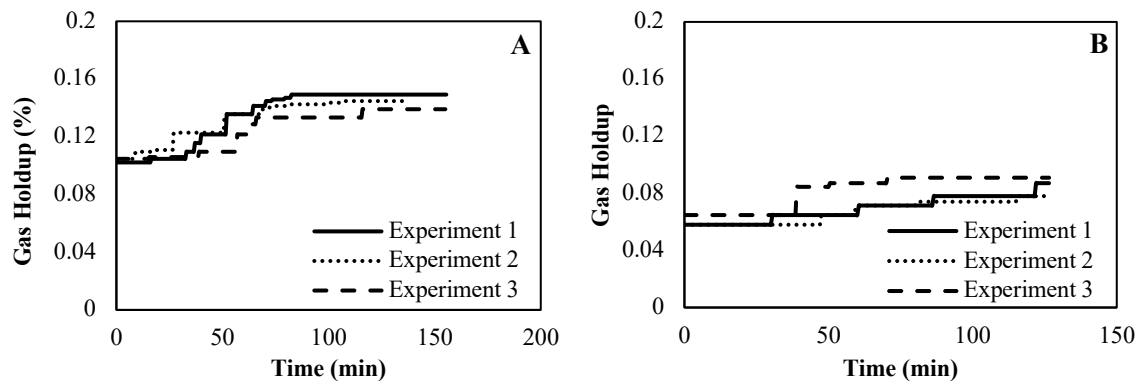


Figure 10. Gas holdup profiles for the glycine/KOH (A) and sarcosine/KOH (B) solutions.

Average Bubble Size and Bubble Size Distribution. The bubble size was determined from frames of video clips taken at different points during each experiment (Figure 11). The maximum and minimum diameters of each bubble measured were averaged and scaled by comparing the bubble sizes to an immersed object of known diameter in the video clip.

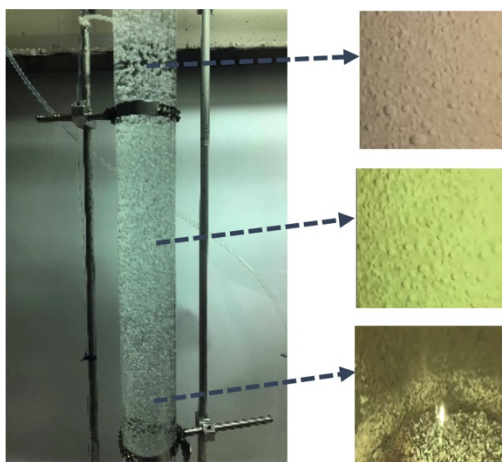


Figure 11. Picture of the actual BCR used in the experiments. The bubble column was divided into three sections based on height and videos were taken at each section to determine the bubble size distribution and average bubble size as functions of height and time.

Figures 12 and 13 illustrate the average bubble size and bubble-size distribution as functions of time and column height in glycine and sarcosine promoted solutions, respectively. Figures 12A and 12B illustrate the average bubble size at a given column height and time for glycine (A) and sarcosine (B). The average bubble size in both amino acid promoted solutions is seen to increase with column height. Furthermore, at a given column height, the average bubble size decreases with time. The increase in bubble size with column height can be attributed to the decrease in pressure, as well as increasing bubble coalescence events, as the bubbles travel up the column. The decrease in bubble size over time at a given column height can be explained by the Marangoni effect, which affects the surface tension gradient when mass transfer from the bubbles to the liquid phase occurs, leading to enhanced bubble coalescence (Tsouris and Tavlarides, 1993). As the solvent becomes saturated with CO_2 , the mass-transfer driving force and the surface tension gradient decrease, thus decreasing the bubble coalescence rate. Initially, when the solvent is CO_2 -lean, the bubble

coalescence rate is highest, leading to higher bubble size. Over time, as the coalescence rate decreases, the bubbles become smaller.

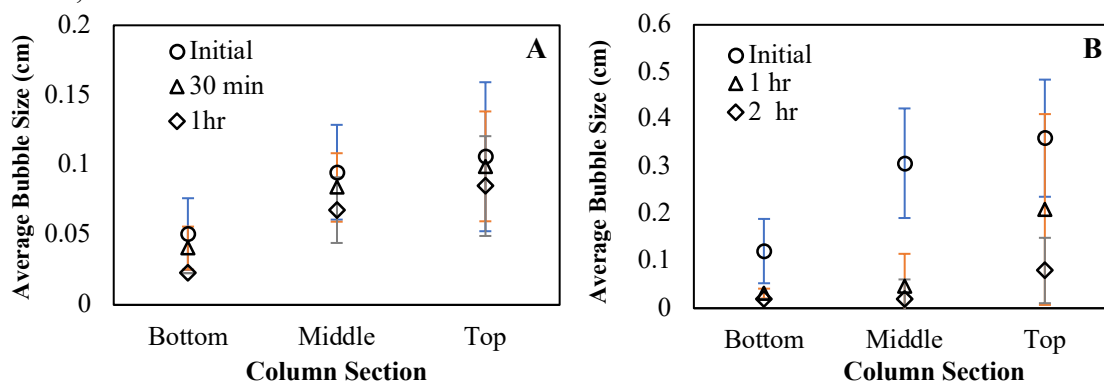


Figure 12. Average bubble size as a function of time and column height: (A) Average bubble size in glycine/KOH sorbent; (B) Average bubble size in sarcosine/KOH sorbent.

The bubble size distributions for glycine promoted KOH vs time and column height are shown in Figure 13.

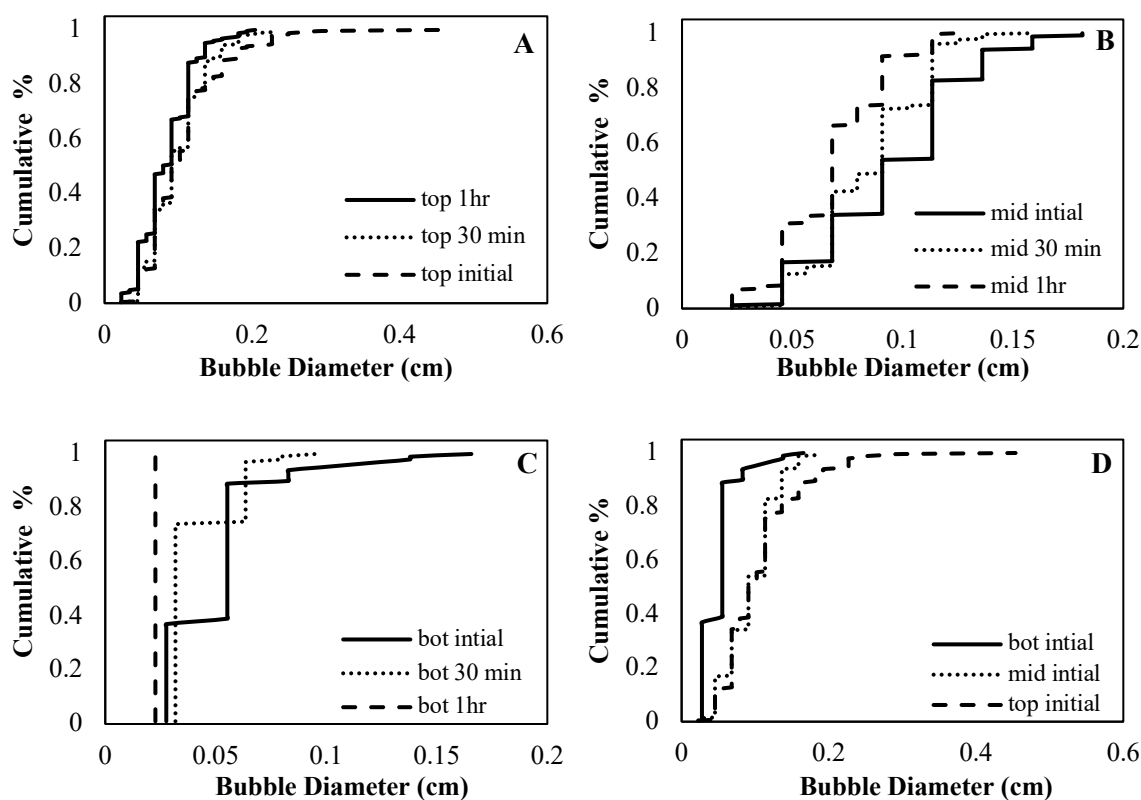


Figure 13. Bubble size distributions in glycine promoted KOH: (A) Bubble size distribution as a function of time, 55 cm from the base of the column; (B) Bubble size distribution as a function of time, 35 cm from the base of the column; (C) Bubble size distribution as a function of time, 15 cm from the column base; (D) Bubble size distribution as a function of column height ($t = \text{initial}$).

Dispersion Coefficient. To calculate the liquid dispersion coefficient in the BCR, which is needed in the process model, we studied the residence time distribution of an injected tracer. A diagram of the experimental setup used for this part of the study can be found in Figure 14. A sodium chloride tracer was prepared by mixing 500 mg of sodium chloride in 20 mL of deionized water. The bubble column reactor was filled with 3L of water. Liquid flowrates of 5.7 mLs⁻¹, 6.1 mLs⁻¹, and 7.4 mLs⁻¹ were used without recycling. Nitrogen gas was introduced through the bubble diffuser at the bottom of the column at three flowrates: 0 Lmin⁻¹, 1 Lmin⁻¹, and 1.9 Lmin⁻¹. The sodium chloride tracer was injected from the top of the column as a short pulse, and the exit concentration profile of sodium chloride was analyzed using a conductivity probe. Data points were taken every 10 seconds for 3 hours. The conductivity of sodium chloride at the exit of the column was measured as a function of time. Then, the measured conductivity was translated into concentration by using calibration measurements of conductivity vs concentration of different sodium chloride solutions. The following relationship between concentration and conductivity was used:

$$\text{Concentration (ppm)} = \text{Conductivity} * 0.4113 + 2.4754 \quad (1)$$

The dispersion coefficient (D_l) was determined by solving the convective transport equation:

$$D_a \frac{\partial^2 c_T}{\partial z^2} - U \frac{\partial c_T}{\partial z} = \frac{\partial c_T}{\partial t} \quad (2)$$

Here, z is the axial-coordinate, c_T is the tracer concentration, u_l is the liquid-phase superficial velocity, and D_l is the liquid-phase dispersion coefficient. The differential equation was solved using the closed-open boundary condition, i.e., $D_l = 0$ before the column entrance and $D_l > 0$ after the column exit.

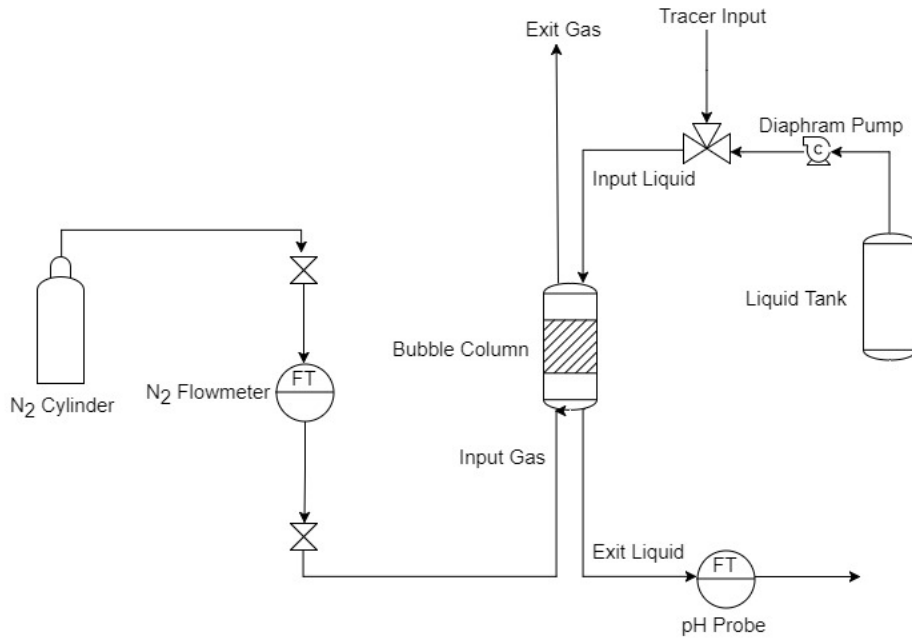


Figure 14. Experimental setup for the tracer study. The tracer (sodium chloride) was injected as a pulse in a water flow introduced at the top of the column, and the exit concentration of sodium chloride was measured using a conductivity probe at the bottom of the column over time.

Figure 15 displays typical experimental tracer data along with the model used to determine the dispersion coefficient. The values of the dispersion coefficients were calculated by solving eq. (2). Table 2 illustrates the effects of liquid and gas flowrates on the dispersion coefficient. It is shown that the liquid flowrate through the bubble column reactor has a negligible effect on the liquid dispersion coefficient. Increasing the flowrate of N₂, however, increases the value of the dispersion coefficient. The negligible effect of liquid flowrate on the dispersion coefficient can be attributed to the fact that the liquid velocity in the column is much smaller than the gas velocity.

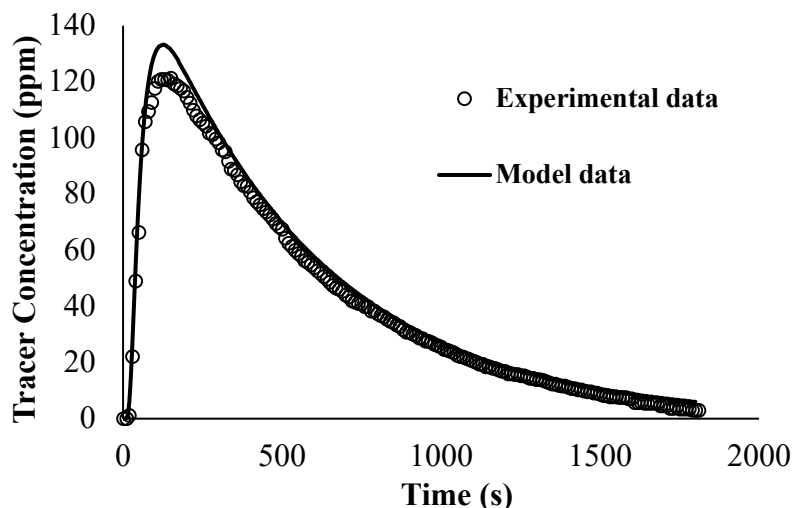


Figure 15. Comparison of experimental residence time distribution data with the model used to determine the value of the dispersion coefficient. The figure shows results for a N₂ flow rate of 1.87 Lmin⁻¹ and a water flow rate of 5.7 mLs⁻¹.

Table 2. Dispersion coefficient as a function of liquid and gas flow rates.

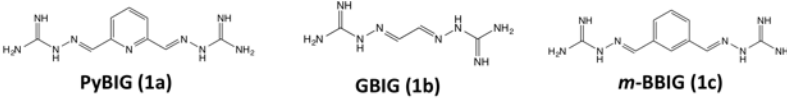
Water Flowrate (mLs ⁻¹)	N ₂ Flowrate (L min ⁻¹)	Dispersion Coefficient (m ² s ⁻¹)
5.72	0	0.003
5.72	1.00	0.0009
5.72	1.87	0.0015
6.11	0	0.0002
6.11	1.00	0.0009
6.11	1.87	0.0015
7.43	0	0.0002
7.43	1.00	0.0009
7.43	1.87	0.0015

Conclusions. Under batch conditions, the parameters required to model the absorption of CO₂ in amino acid/potassium hydroxide sorbent, namely the dispersion coefficient, gas phase holdup, and bubble size distribution, were characterized. The dispersion coefficient of the BCR was found to be independent of the liquid flowrate and increased with increasing gas flowrate. The negligible effect of increasing liquid flowrate can be attributed to the magnitude in difference between liquid and gas volumetric flowrates. The gas-phase holdup was observed to increase with time until steady state was reached. The average bubble size in both glycine and sarcosine solutions increases

with column height. The average bubble size in both solutions at a given column height decreases over the course of the reaction mainly due to a decrease in the bubble coalescence rate as the mass-transfer driving force decreases with time. Experimental information obtained in this part of the study was used to develop and evaluate a mathematical model that can be used to predict the performance of the column over a wide range of operating parameters. The model will be first employed to predict the CO₂ breakthrough behavior, and simulation results will be compared to experimental data.

3.5 Sorbent Regeneration by Guanidine Crystallization

The objectives of this task were to select an ideal guanidine compound, identify the optimal conditions for the crystallization of the guanidinium (bi)carbonate salts, effectively integrate the crystallization stage into the overall CO₂ capture and release process, and optimize the sorbent and guanidine ligand regeneration. Three guanidine compounds were considered for this project, as shown in Figure 1. Specifically, they are bis-iminoguanidine ligands (BIGs) that were previously found to crystallize with (bi)carbonate anions into insoluble solids. While guanidines **1a** and **1b** react with CO₂ and form crystalline carbonate (**2a**) and bicarbonate (**2b**) salts, respectively, guanidine **1c** forms an amorphous carbonate solid (**2c**). We tested all three BIG compounds for their ability to remove (bi)carbonate from the loaded glycine and sarcosine solvents by crystallization, and compared other relevant characteristics, such as gravimetric CO₂ capacity of the crystalline (bi)carbonate salts, enthalpy of CO₂ release from the (bi)carbonate crystals, CO₂ release time (from the crystals), and cost of synthesis (Figure 16).



Carbonate	PyBIG(CO ₃)(H ₂ O) ₄	GBIG(HCO ₃) ₂ (H ₂ O) ₂	m-BBIG(CO ₃)(H ₂ O) ₄
CO ₂ capacity (wt%)	11.5	26.6	11.6
Cyclic capacity (gly/sar) mol CO ₂ /mol amino acid	0.21/0.26	0.20/0.27	0.23/0.29
Cost (\$/kg)	>1000	3	3
ΔH CO ₂ release (kJ/mol)	223	121.5	167
CO ₂ release time (120 °C)	9 min	3 min	9 min

Figure 16. Comparison of relevant characteristics of BIG sorbents **1a-c**.

All BIG ligands performed relatively well in regenerating the glycine and sarcosine amino acids, with measured capacities in the range of 0.2-0.3 mol CO₂/mol amino acid. Guanidine compound **1a**, however, is very expensive to make and has a relatively large enthalpy of CO₂ release. **1c**, on the other hand, can be made relatively cheaply, but its enthalpy of CO₂ release is significantly higher compared to **1b**. Finally, **1b** has more than twice as large gravimetric CO₂ capacity than **1a** and **1c**, as it binds the CO₂ as bicarbonate anions (vs carbonate for **1a** and **1c**). Finally, stability tests showed virtually no decomposition of **1b** after heating in air at 120 °C for 1 week. Based on these preliminary tests, we selected guanidine compound **1b** for further study and optimization.

Regeneration of the CO₂-loaded glycine and sarcosine amino acids can be effectively done by crystallization with GBIG, which gradually dissolves into solution and recrystallizes as

GBIGH₂(HCO₃)₂(H₂O)₂. In this process, the basic guanidine groups of GBIG deprotonate the zwitterionic forms of the loaded amino acids, converting them back into the active anionic forms. The resulting GBIGH₂²⁺ cations crystallize with the HCO₃⁻ anions, removing them from solution, thereby unloading the CO₂ from the sorbent. The reaction reaches equilibrium state when the pH of the solution becomes high enough (≈ 10 -10.2) that the guanidine groups of GBIG are mostly deprotonated and thus unable to crystallize with the bicarbonate anions. The regeneration is mostly driven by the solubility difference between GBIG and GBIGH₂(HCO₃)₂(H₂O)₂, which is a function of the bicarbonate concentration and the solution pH. The amount of CO₂ removed from solution during sorbent regeneration essentially corresponds to the cyclic capacity of the amino acid sorbent. Once removed from solution, the GBIGH₂(HCO₃)₂(H₂O)₂ crystals can be heated in the solid state at 120 °C to release the CO₂ and H₂O and regenerate GBIG quantitatively.

The glycine or sarcosine amino acids were regenerated by adding 0.25 molar equivalents of solid GBIG and stirring the resulting slurries at room temperature for 2 hours. The concentrations of carbonate and carbamate in solutions were monitored by IC and ¹H NMR spectroscopy, respectively. The total amount of CO₂ removed as a function of time is plotted in Figure 17. Most of the regeneration occurred in the first 20 min, and longer stirring times only resulted in minimal increases in the CO₂ removed, which indicates the equilibrium state is reached relatively quickly despite the three-phase reaction. Under these conditions, the corresponding cyclic CO₂ capacities for glycine and sarcosine are 0.33 ± 0.05 and 0.31 ± 0.05 mol/mol, respectively.

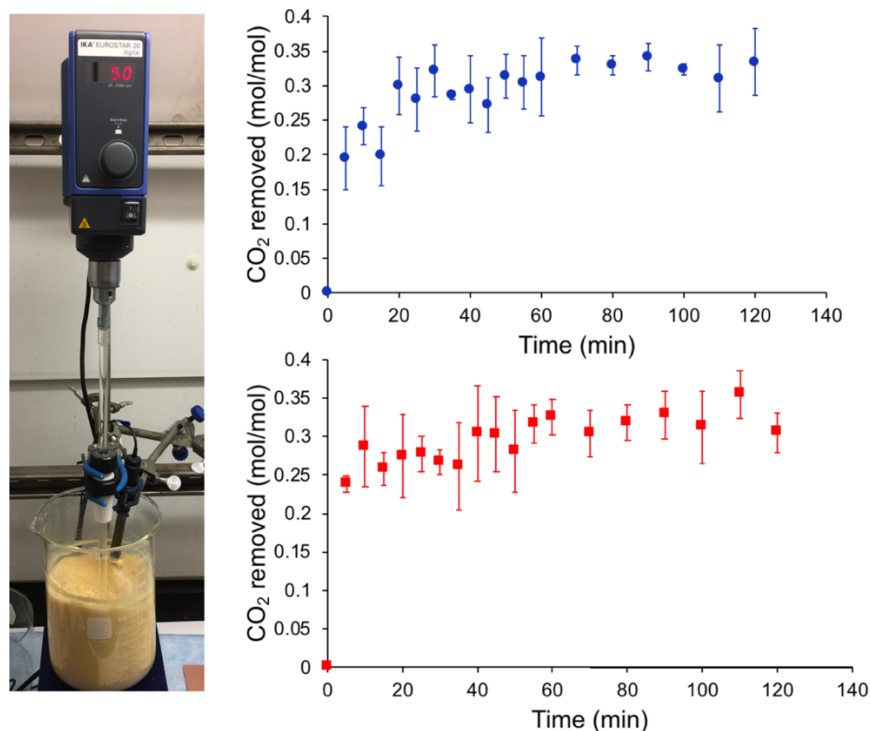


Figure 17. Time-dependent regeneration of glycine (blue dots) and sarcosine (red squares) by GBIGH₂(HCO₃)₂(H₂O)₂ (**2b**) crystallization. Solid GBIG was mixed with the loaded amino acid solutions, and the resulting slurries were stirred for 2 hrs. The amounts of CO₂ removed relative to the amino acids in solution (mol/mol) were monitored by measuring the (bi)carbonate and carbamate concentrations left in solution. The error bars are defined as the standard deviations from three separate regeneration experiments.

3.6 CO₂ Separation Cycles

Any sustainable CO₂ capture process requires efficient sorbent recycling over multiple absorption-release cycles. A complete CO₂ separation cycle with amino acid/GBIG consists of loading the glycine or sarcosine sorbent with the bubble reactor, adding the GBIG solid to the loaded sorbent and stirring the suspension for 2 hours, then filtering the solid to separate the GBIG-bicarbonate crystals and the regenerated amino acid solution. Finally, the GBIG-bicarbonate crystals are heated for 2 hrs at 120 °C in an oven to release the CO₂ and regenerate GBIG (Figure 18). The recovered amino acid and GBIG are then reused in another cycle. We ran 5 and 4 consecutive cycles with glycine and sarcosine, respectively, and the measured cyclic capacities are plotted in Figure 19. While there was some variation from one cycle to another, the cyclic capacities stayed relatively constant within the 0.2-0.3 mol/mol range.

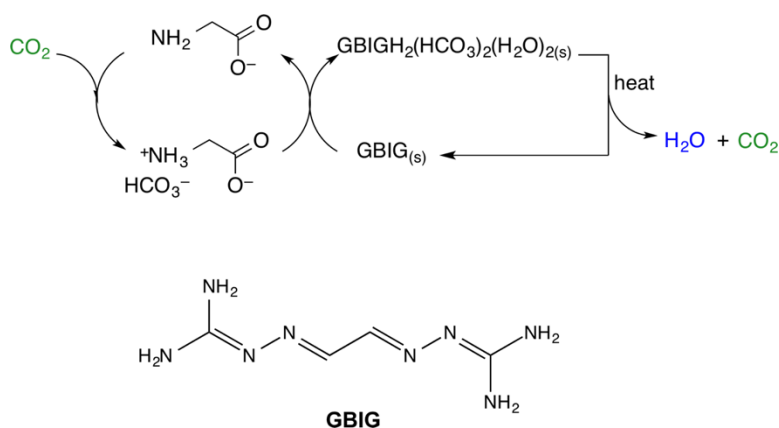


Figure 18. CO₂ separation cycle combining CO₂ absorption by an aqueous amino acid salt (e.g., glycine) and bicarbonate crystallization with GBIG (**1b**).

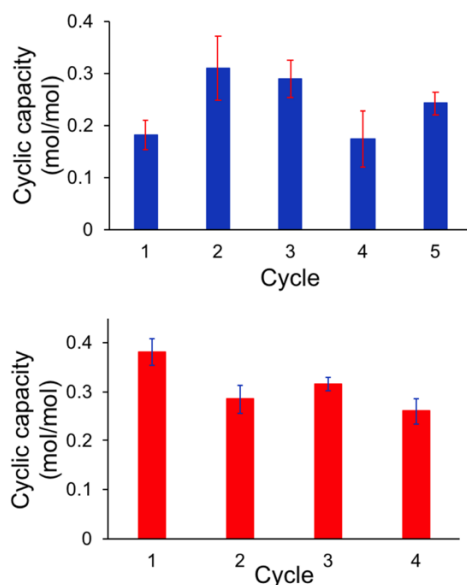


Figure 19. Measured cyclic capacities for glycine (top) and sarcosine (bottom) with GBIG (**1b**) for consecutive loading/regeneration cycles.

By adding the additional crystallization step, this hybrid solvent/solid-state approach circumvents the energy-intensive processes of heating and boiling aqueous solutions, typically involved in traditional solvent-based carbon capture methods. This results in a significantly lower regeneration energy compared to industrial benchmarks like aqueous monoethanolamine (MEA) or sodium glycinate (SG), as summarized in Table 3 and depicted in Figure 20. In this energetic comparison, the total regeneration energy can be broken down into its three components: 1) the reaction enthalpy, or the heat required to chemically desorb the CO₂ from the sorbent, 2) the sensible heat, or the energy required to heat the sorbent from ambient conditions to the CO₂-release temperature and 3) the heat of vaporization, or the energy involved in boiling and evaporating the aqueous sorbent (Song, 2008). Despite the higher reaction enthalpy required for the CO₂ release, overall the glycine/sarcosine + GBIG system requires 24% and 40% less energy than the MEA and SG benchmarks, respectively. This is a direct consequence of the much lower sensible heat of crystalline GBIGH₂(HCO₃)₂(H₂O)₂ compared to aqueous MEA and SG, and that no solvent evaporation is involved (technically, two equivalents of water vapors are released from the GBIG-bicarbonate crystals for each equivalent of CO₂ released, but that energy is already accounted for as part of the reaction enthalpy). Finally, another potential advantage of the hybrid glycine/sarcosine + GBIG system is that by avoiding heating and boiling the amino acid solutions, sorbent loss through evaporation and degradation is minimized.

Table 3. Minimum regeneration energy (kJ/kg CO₂) required for the hybrid potassium glycinate/sarcosinate + GBIG system compared to the 30% aqueous monoethanolamine (MEA) and 30% aqueous sodium glycinate (SG) benchmark sorbents.

	MEA ^a	SG ^b	Gly/Sar + GBIG ^c
Reaction enthalpy	1636	1568	2761
Sensible heat	2191	3220	682
Heat of vaporization	676	955	–
Total energy	4503	5743	3443

^aGottlicher, 2004. ^bSong, 2008. ^cWilliams, 2019.

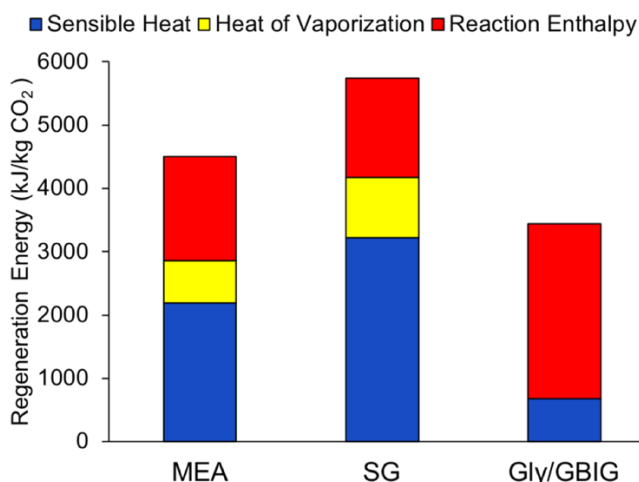
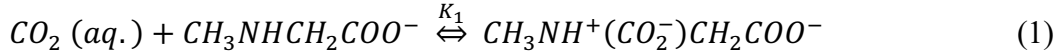


Figure 20. Minimum regeneration energy requirements (kJ/kg CO₂) for the glycine/GBIG hybrid system compared to 30% aqueous monoethanolamine (MEA) and 30% aqueous sodium glycinate (SG) benchmarks.

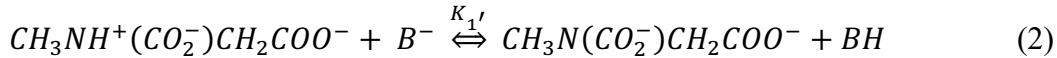
4. MODELING RESULTS AND DISCUSSION

The goal of this computational work was to develop dynamic models to simulate CO₂ absorption by using amino acid solutions as absorption solvents, which have the potential to reduce the amount of energy required by the regeneration process. A reaction scheme is proposed to represent the chemical reactions between the amino acid and CO₂. Two reaction models for a two-phase batch reactor and a bubble column, based upon transient mass and energy balances for the chemical species found in CO₂ gas-liquid absorption, are presented. Computer codes have been written to implement the proposed models. Simulation results are presented and discussed. The proposed models can be used to optimize and control CO₂ absorption in practical applications.

Reaction Scheme. The most important part of the proposed model is the simulation of the complex chemical reactions involving selected amino acid salts, solvents, and CO₂. In the case of sarcosine (CH₃NHCH₂COO⁻) several authors (Portugal et al., 2007; Simons et al., 2010; Xiang et al., 2012; and Mahmud et al., 2017) have studied the kinetics and proposed a mechanism similar to the originally proposed by Caplow (1968) and reintroduced by Danckwerts (1979) for primary and secondary amines. CO₂ reacts with the amino acid through a two-step process. The first step proceeds through the formation of a zwitterion intermediate:



This step is slow and considered to be the rate controlling step. It is followed by a very fast removal of a proton by a base:



It is important to notice that all bases present in the liquid phase will participate in reaction (2); therefore, B_i represents a generic base participating in the reaction with the zwitterion. In this mechanism, the overall forward reaction rate equation can be derived using the quasi-steady-state assumption for the zwitterion intermediate (Versteeg and van Swaaij, 1988; and others):

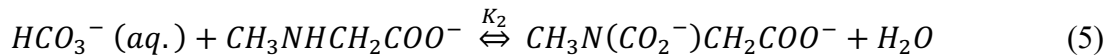
$$r_1 = \frac{k_1[CO_2][CH_3NHCH_2COO^-]}{1 + \frac{k_{-1}}{\sum_i k_{bi}[B_i]}} \quad (3)$$

In eq. (3), k_1 , k_{-1} , and k_{bi} are the respective specific constants, and $\sum_i k_{bi}[B_i]$ represents the summation over the reaction rates of all the bases reacting with the zwitterion present in the solution. In the case of high amine concentration in the solvent, eq. (3) is simplified to:

$$r_1 = k_1[CO_2][CH_3NHCH_2COO^-] \quad (4)$$

In the case of amino acid solutions, the overall reaction rate is of second order, and is of first order with respect to the amino acid. This finding indicates that the deprotonation of the zwitterion by the bases present in the solution is very fast compared to the reverse reaction. Therefore, eq. (4) is considered the main reaction in the absorption of CO₂ in high concentration aqueous amino acid solutions.

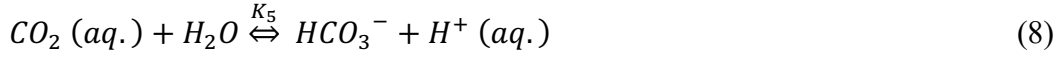
The amino acid molecules also react with bicarbonate to generate carbamate ions by:



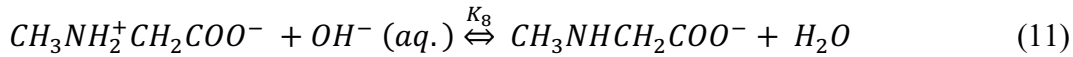
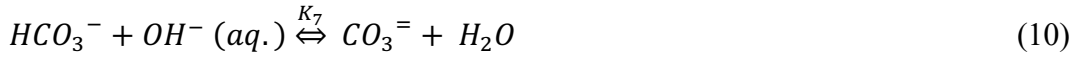
The carbamate ions generated in reaction (2) participate in a pH limited reaction to generate protonated carbamate ions by:



In all the cases discussed above the following CO₂ reactions are also present:



Reaction (8) is very slow and can be neglected in most circumstances. Reaction (7), however, is fast and can enhance mass transfer even when the concentration of the hydroxyl ion is low (Bosch et al., 1989). The reaction scheme is completed by including the following reactions:



Reaction (9) allows calculation of pH throughout the process. Reaction (10) reflects the fact that, at high pH, the carbonate ion concentration is much higher than that of the bicarbonate ion. The equilibrium between the neutral and alkaline (salt) forms of the amino acid is represented by eq. (11). A list of all reactions is included in the Appendix. All chemical compounds participating in the reaction scheme are listed in Table AI. Kinetic data were collected from the literature, and the values of the kinetic constants are listed in Table AII in the Appendix.

The generation terms (R_{geni}), which appear in the mass balances for the two reactive systems, are calculated assuming pseudo-steady state for every chemical species. In order to simplify the calculations, we determined an overall rate per reaction according to:

$$R_{ai} = r_{if} - r_{ir} \quad (12)$$

Every generation term (R_{geni}) is calculated from eqs (1) to (11) by a molar balance using:

$$R_{gen1} = - 2 R_{a1} - R_{a2} + R_{a8} \quad (13)$$

$$R_{gen2} = R_{a1} - R_{a3} \quad (14)$$

$$R_{gen3} = R_{a3} \quad (15)$$

$$R_{gen6} = - R_{a2} + R_{a4} + R_{a5} - R_{a7} \quad (16)$$

$$R_{\text{gen}7} = -R_{a4} + R_{a6} \quad (17)$$

$$R_{\text{gen}8} = -R_{a3} + R_{a5} + R_{a6} \quad (18)$$

$$R_{\text{gen}9} = R_{a7} \quad (19)$$

$$R_{\text{gen}10} = R_{a8} \quad (20)$$

Reactive Mass Transfer. In this work, we represent the gas-liquid reactive mass transfer using the two-film model (Lewis and Whitman, 1924). The model assumes that interphase mass transfer occurs only by molecular diffusion in two thin layers on both sides of the interphase. The concentration in the bulk of the gas and liquid phases outside the thin layers remains constant. The model also assumes a linear concentration driving force in both layers (Morsi and Basha, 2017). This model leads to the definition of mass transfer coefficients in each thin layer (k_g and k_l). The increased transport due to the presence of the chemical reaction is accounted for by using an enhancement factor (E) defined as the ratio of mass transfer with and without chemical reaction (Richardson et al., 2008). Commonly, the value of the enhancement factor is estimated as a function of the Hatta number (Ha) using the numerical solution proposed by van Krevelen and Hoftijzer (1948).

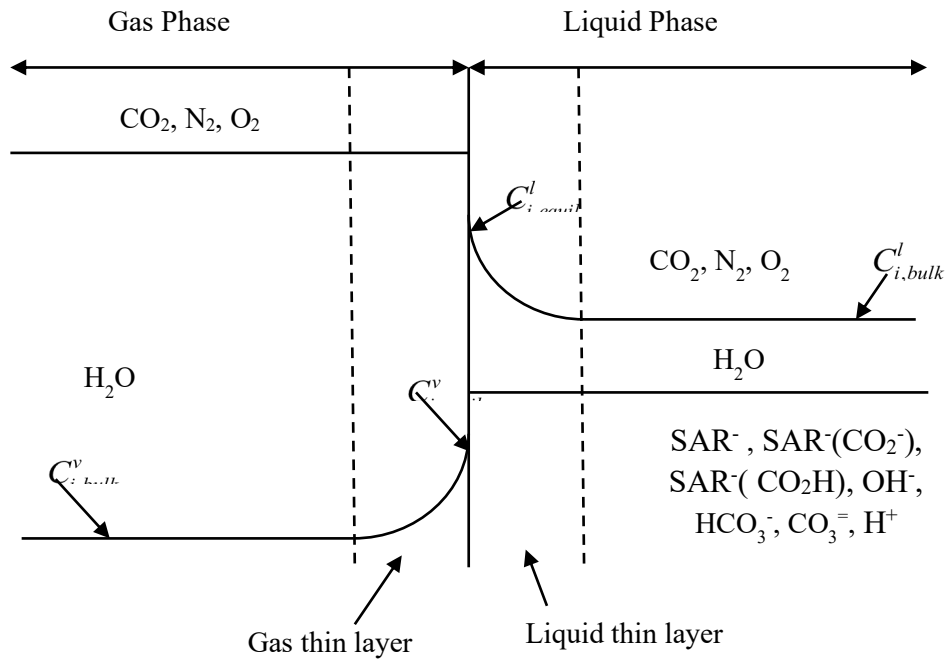


Figure 21. Concentration gradients at the vapor-liquid interphase.

The components in the gas phase are CO_2 , H_2O , N_2 , and O_2 while the species considered in the liquid phase are: SAR^- , $\text{SAR}^-(\text{CO}_2^-)$, $\text{SAR}^-(\text{CO}_2\text{H})$, OH^- , HCO_3^- , $\text{CO}_3^{=}$, H^+ . The ionic species remain in liquid phase, while the others are transferred from one phase to the other according to the scheme shown in Figure 21.

Gas phase mass transfer resistance is considered for water, the only volatile liquid solvent, while liquid only mass-transfer resistance for the gas species has been considered for CO₂, N₂, O₂ (Greer, 2008; among others). Under certain conditions, however, both resistances have to be considered for the reacting species CO₂. In the implementation of our model, we consider these situations by using a global mass transfer coefficient given by:

$$\frac{1}{K_{CO_2}^l} = \frac{1}{E k_{CO_2}^l} + \frac{H^{cc}}{k_{CO_2}^g} \quad (21)$$

Here, $K_{CO_2}^l$ is the overall mass transfer coefficient based upon liquid phase concentrations, $k_{CO_2}^l$ is the liquid-phase mass-transfer coefficient, $k_{CO_2}^g$ is the gas-phase mass-transfer coefficient, $H^{cc} = C_i^l/C_i^g$ is the concentration based Henry's constant, C_i^l and C_i^g are the liquid and gas phase species concentrations, respectively, and E is the enhancement factor defined by Richardson et al. (2008). The CO₂ molar flow term ($N_{CO_2,diff}$) is given by (Bedelbayev et al., 2008; Greer et al., 2008; and Greer, 2008):

$$N_{CO_2,diff} = -k_{CO_2}^l E a_w H^{cc} C_{CO_2}^g \quad (22)$$

Here, a_w is the interphase area per unit volume. The enhancement factor (E) is a function of the Hatta number (Ha) defined as:

$$Ha = \frac{\sqrt{D_{CO_2}(k_{1f} C_{AMA} + k_{3f} C_{OH^-} + k_{4f} C_{H_2O})}}{k_l} \quad (23)$$

D_{CO_2} is the diffusion coefficient and k_{if} are the forward specific reaction rate constants. The influence of the different reactions on the total rate of CO₂ absorption is considered by the enhancement factor E . The Ha number is the ratio of the rate of homogeneous reaction relative to the rate of gas dissolution. Ha is also a measure of the amount of dissolved gas that reacts inside the diffusion film near the gas-liquid interface compared to the amount that reaches the bulk of the solution without reacting. When $Ha = 0$, we have purely physical absorption. The higher the value of the Hatta number, the stronger is the effect of chemical reactions on mass transfer. In the case of $Ha > 2$, the enhancement factor E is directly equal to the Ha number (Perry and Green, 1999).

4.1 Two-Phase Batch Reactor Modeling

Mass Balances. Instantaneous reaction and ideal mixing inside the reactor were assumed for the reactor model. Therefore, the concentrations are assumed constant throughout the reactor and equal to the corresponding concentrations in the exiting stream. In the batch reactor depicted in Figure 22a, we carried out the mass balance of component i in the liquid phase using (Greer, 2008; Gabitto and Tsouris, 2018):

$$\frac{\partial C_i^l}{\partial t} = N_{i,diff} + R_{gen,i} (1 - \varepsilon_g) \quad (24)$$

$$N_{i,diff} = k_l E a_w (C_i^{l,*} - C_i^l) \quad (25)$$

$$\frac{\partial C_i^l}{\partial t} = k_l E a_w (C_i^{l,*} - C_i^l) + R_{gen,i} (1 - \varepsilon_g) \quad (26)$$

Here, $C_i^{l,*}$ is the liquid phase equilibrium concentration at the gas-liquid interphase, ε_g is the gas hold-up (V_g/V_T), $R_{gen,i}$ represents moles of species i generated/consumed by interphase reaction per unit volume, and $N_{i,diff}$ is the molar flow of component i from the gas into the liquid phase. In the cases of ionic species, there is no interphase mass transfer; therefore, for these reactions, eq. (24) becomes:

$$\frac{\partial C_i^l}{\partial t} = R_{gen,i} (1 - \varepsilon_g) \quad (27)$$

In the gas phase a mass balance for species i leads to:

$$\frac{\partial C_i^g}{\partial t} = -N_{i,diff} + \frac{\dot{V}}{V_R} (C_{i,In}^g - C_{i,Out}^g) \quad (28)$$

We replace $N_{i,diff}$ using eq. (25) to obtain:

$$\frac{\partial C_i^g}{\partial t} = \frac{u_g}{H} (C_{i,In}^g - C_{i,Out}^g) - k_l a_w (C_i^{l,*} - C_i^l) \quad (29)$$

Here, H is the reactor height, u_g is the gas superficial velocity, and $C_{i,In}^g, C_{i,Out}^g$ are the input and output gas phase concentrations of component i , respectively.

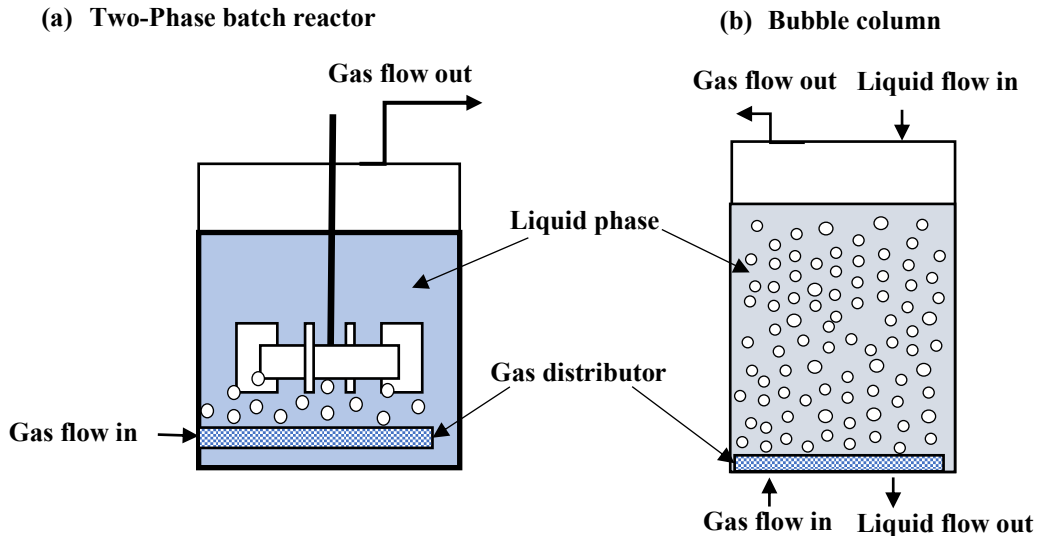


Figure 22. Different reactor configurations: (a) two-phase batch reactor and (b) bubble column.

Parameter Estimation. The implementation of the proposed two-phase batch reactor model requires the evaluation of several parameters including the overall gas hold-up ε_g , the volumetric mass transfer coefficient $k_l a_w$, the liquid-side mass-transfer coefficient k_l , the volumetric interfacial area a_w , the bubble size d_{bs} , and bubble distribution. We initially estimated the values of these parameters by using experimental correlations reported in the literature.

The overall gas hold-up (ε_g) was calculated using the following correlation (Bouaifi et al., 2001):

$$\varepsilon_g = 22.4 (P_g/V_l)^{0.24} u_g^{0.65} \quad (30)$$

Here, V_l is the liquid phase volume and P_g is the power consumption given by (Luan et al., 2017):

$$P_g/P_o = 0.309 + 0.691 \exp(-0.00205 F_l^{1.556}) \quad (31)$$

where F_l is the dimensionless gas flow number and P_o is the power consumed by the impeller in the absence of the gas phase. These parameters were calculated using:

$$F_l = \frac{Q_g}{N d_i^3} \quad (32)$$

$$P_o = N_p \rho_l N^3 d_i^5 \quad (33)$$

In eqns. (32) and (33), Q_g is the gas-phase volumetric flowrate, ρ_l is the liquid-phase density, N is the impeller rotational speed (rpm), d_i is the impeller diameter, and N_p is the power number given by:

$$N_p = 6.59 - 54.771 (b_i/d_i) \quad (34)$$

Here, b_i is the height of the impeller blade.

The diameter of the bubbles was calculated using (Lee and Meyrick, 1970):

$$d_{bs} = 4.25 \frac{\sigma_l^{3/5}}{\rho_l^{3/5} (P_g/V_l)^{2/5}} \varepsilon_g^{1/2} \quad (35)$$

Here, σ_l is the liquid phase surface tension.

The specific interphase area (a_w) can be calculated from the values of the gas hold-up and bubble size diameter as:

$$a_w = \frac{6 \varepsilon_g}{d_{bs} (1 - \varepsilon_g)} \quad (36)$$

The liquid side mass transfer coefficient is calculated from (Bouaifi et al., 2001):

$$k_l a_w = 0.0218 (P_g/V_l)^{0.55} u_g^{0.6} \quad (37)$$

Energy Balances. Some of the chemical reactions given in the reaction scheme are highly exothermic; therefore, an energy balance has to be solved in order to consider temperature changes. The values of the heat of reaction used in equations (1) and (7) were 60 kJ/molCO₂ and 20 kJ/molCO₂, respectively. The first value was taken from Xiang (2012) and the second from Pinsent et al. (1956).

A two-equation model for a transient energy balance leads to the following equations Greer et al., 2008; Lawal et al., 2009):

$$\frac{\partial T^l}{\partial t} = -N_{CO_2,diff} \frac{\Delta H_R}{\sum_i C_i^l C_{pi}^l} - U_T a_w \frac{(T^l - T^g)}{\sum_i C_i^l C_{pi}^l} \quad (38)$$

$$\frac{\partial T^g}{\partial t} = U_T a_w \frac{(T^l - T^g)}{\sum_i C_i^g C_{pi}^g} \quad (39)$$

Here, C_{pi}^g and C_{pi}^l are the heat capacities of component i in the mixture, U_T is the global heat transfer coefficient, and ΔH_R is the heat released by the chemical reaction. The CO_2 molar flow term ($N_{CO_2,diff}$) is given by eq. (22), while the enhancement factor (E) is given by the Hatta number defined by eq. (23).

4.2 Bubble Column Modeling

Mass Balances. For the bubble column reactor depicted in Figure 22b, we carried out the mass balance of component i in the liquid phase for a differential balance using (Greer, 2008; Tavlarides et al., 2015):

$$\frac{\partial C_i^l}{\partial t} = (1 - \varepsilon_g) D_l \frac{\partial^2 C_i^l}{\partial z^2} + u_l \frac{\partial C_i^l}{\partial z} + N_{i,diff} + R_{gen,i} (1 - \varepsilon_g) \quad (40)$$

Here, u_l is the liquid-phase superficial velocity and D_l is the liquid-phase dispersion coefficient. Replacing the interfacial mass transfer ($N_{i,diff}$) using eq. (25) leads to:

$$\frac{\partial C_i^l}{\partial t} = (1 - \varepsilon_g) D_l \frac{\partial^2 C_i^l}{\partial z^2} + u_l \frac{\partial C_i^l}{\partial z} + k_l E a_w (C_i^{l,*} - C_i^l) + R_{gen,i} (1 - \varepsilon_g) \quad (41)$$

A mass balance for species i in the gas phase leads to:

$$\frac{\partial C_i^g}{\partial t} = \varepsilon_g D_g \frac{\partial^2 C_i^g}{\partial z^2} - u_g \frac{\partial C_i^g}{\partial z} - N_{i,diff}^l \quad (42)$$

We replace $N_{i,diff}$ using eq. (25) to obtain:

$$\frac{\partial C_i^g}{\partial t} = \varepsilon_g D_g \frac{\partial^2 C_i^g}{\partial z^2} - u_g \frac{\partial C_i^g}{\partial z} - k_l a_w (C_i^{l,*} - C_i^l) \quad (43)$$

Parameter Estimation. Implementation of the proposed bubble column model requires the evaluation of the overall gas hold-up ε_g , the volumetric mass transfer coefficient $k_l a_w$, the liquid-side mass-transfer coefficient k_l , the volumetric interfacial area a_w , the gas and liquid dispersion coefficients D_g and D_l , the bubble size d_{bs} and the bubble distribution throughout the column. We estimated the values of these parameters by using experimental correlations reported in the literature. We also used experimental measurements of these parameters in our calculations, with results reported elsewhere (Kasturi et al., 2018).

The overall gas hold-up (ε_g) was calculated using the following correlation (Hikita and Kikukawa, 1974):

$$\varepsilon_g = 0.505 (0.072/\sigma_l)^{0.6667} (0.001/\mu_l)^{0.05} u_g^{0.47} \quad (44)$$

The specific interphase area (a_w) was calculated from (Akita and Yoshida, 1974):

$$a_w = \frac{0.23}{d_c} \left(\frac{g d_c^2 \rho_l}{\sigma} \right)^{0.5} \left(\frac{g d_c^3 \rho_l^3}{\mu_l^2} \right)^{0.12} \left(\frac{u_g^2}{g d_c} \right)^{0.25} \varepsilon_g \quad (45)$$

The diameter of the bubbles (d_{bs}) was calculated using (Wilkinson et al., 1994):

$$\left(\frac{g \rho_l d_{bs}^2}{\sigma_l} \right) = 8.8 \left(\frac{u_g \mu_l}{\sigma_l} \right)^{-0.04} \left(\frac{\rho_l \sigma_l^3}{g \mu_l^4} \right)^{-0.12} \left(\frac{\rho_l}{\rho_g} \right)^{0.22} \quad (46)$$

The liquid-side mass-transfer coefficient ($k_l a_w$) was calculated from (Hikita et al., 1981):

$$k_l a_w = 14.9 \left(\frac{u_g \mu_l}{\sigma} \right)^{1.76} \left(\frac{g \mu_l^4}{\rho_l \sigma^3} \right)^{-0.248} \left(\frac{\mu_l}{\rho_l D_{g/l}} \right)^{-0.604} \quad (47)$$

Here, $D_{g/l}$ is the diffusivity between the gas and liquid phases.

The liquid axial dispersion coefficient was calculated from (Shah et al., 2012):

$$\left(\frac{u_l d_c}{(1-\varepsilon_g) D_l} \right) = 1.5 \left(\frac{u_l}{\sqrt{g d_c}} \right)^{0.56} \left(\frac{u_g}{\sqrt{g d_c}} \right)^{-0.74} \left(\frac{g \rho_l^2 d_c^3}{\mu_l^2} \right)^{-0.016} \quad (48)$$

Energy Balances. A two-equation model for a transient energy balance leads to the following equations for all the components shown in Figure 1 (Greer et al., 2008; Lawal et al., 2009; Gabitto and Tsouris, 2018):

$$\frac{\partial T^l}{\partial t} = u_l \frac{\partial T^l}{\partial z} - N_{CO_2, diff} \frac{\Delta H_R}{\sum_i c_i^l c_{pi}^l} - U_T a_w \frac{(T^l - T^g)}{\sum_i c_i^l c_{pi}^l} \quad (49)$$

$$\frac{\partial T^g}{\partial t} = -u_g \frac{\partial T^g}{\partial z} - U_T a_w \frac{(T^l - T^g)}{\sum_i c_i^g c_{pi}^g} \quad (50)$$

Eqs (49) and (50) are used to determine the axial temperature profile in both fluid phases.

4.3 Modeling Discussion

Two-Phase Batch Reactor Results. A computer code was developed to implement the model presented in the theoretical section. Table AII in the appendix contains the kinetic data used in all the calculations, while Table AIII contains the main set of data used in the calculations. Typical results are plotted in Figures 23 to 26.

In Figure 23, the output concentration of CO₂ in the gas phase is plotted vs time. At short times, the CO₂ gas phase concentration remains very low until there is a sharp increase at around 20

minutes. At longer times, there is a continuous increase in the calculated CO₂ concentration until a final value equal to the input concentration is reached.

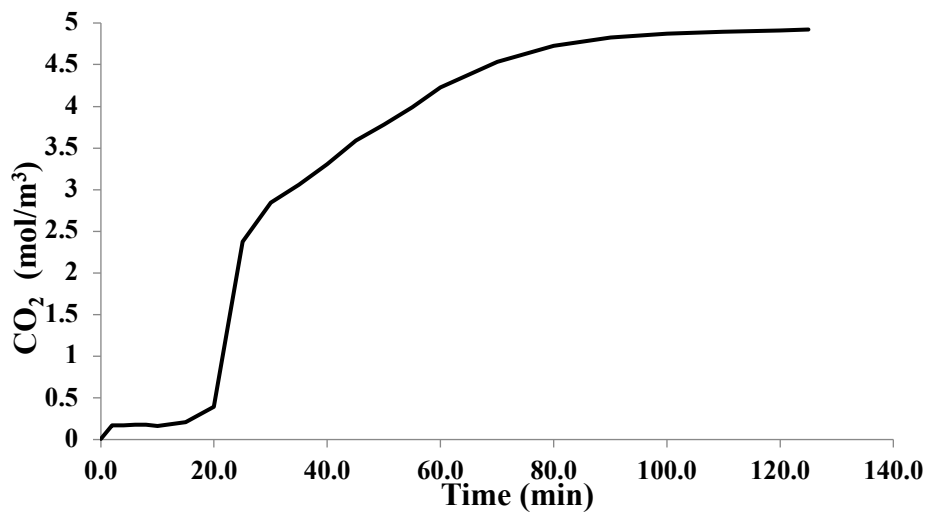


Figure 23. Carbon dioxide breakthrough curve.

In Figure 24, the pH variation is plotted as a function of time. There is a sharp decrease in the pH value until breakthrough occurs. Before breakthrough, the H⁺ ion concentration increases by approximately three orders of magnitude, from 10⁻¹² to 10⁻⁹M. After the breakthrough point, the pH value decreases at a lower rate. The drop in pH affects the equilibrium between the salt (*SAR*⁻) and neutral (*SARH*) forms of the amino acid. A lower pH favors the neutral form over the salt form. Portugal et al. (2007) reported that the neutral form is up to two orders of magnitude less active than the salt form; therefore, the pH drop slows down the amino acid reaction with CO₂.

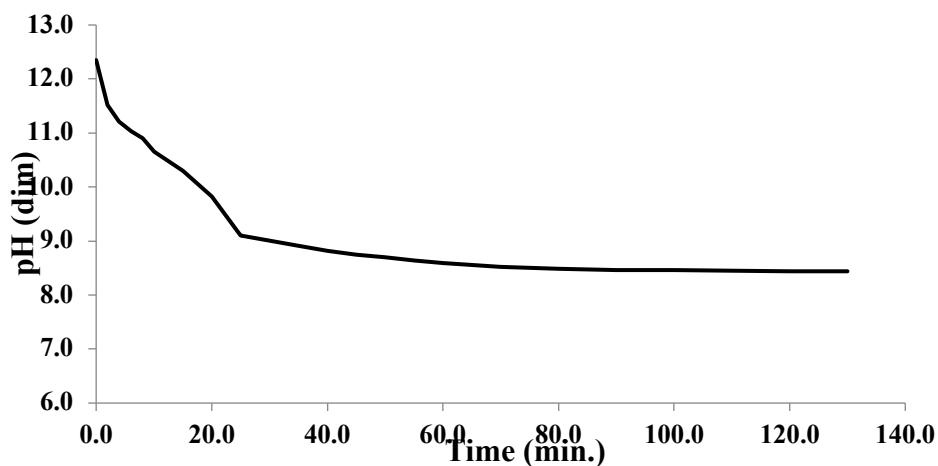
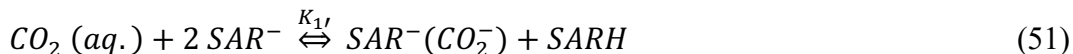


Figure 24. Time variation of pH.

To study the interactions among the different chemical species that appear in the reaction scheme, we plot the concentration of the amino acid forms, salt and neutral, plus the carbamate [*SAR*⁻(*CO*₂⁻)] and protonated carbamate [*SAR*⁻(*CO*₂*H*)] products of the reaction with carbon

dioxide in Figure 25. The mechanism of the reaction between the amino acid and CO_2 , i.e., reactions (1) to (3), has been discussed in the reaction scheme section. The salt form of the amino acid is the most concentrated base present in the solution; therefore, it is expected to be the primary base participating in reaction (3), the zwitterion decomposition. In this case, the reaction between CO_2 and sarcosine can be written as:



Inspection of eq. (51) shows that two molecules of the salt form of the amino acid react with CO_2 and one molecule of the protonated form is produced. Reaction (11) shows that, at short times, due to high pH, the protonated form will be transformed into the salt form. However, Figure 24 shows that this process will slow down rapidly due to the big drop in pH as time increases. After breakthrough, this process is almost negligible. The results plotted in Figure 25 confirm these conclusions.

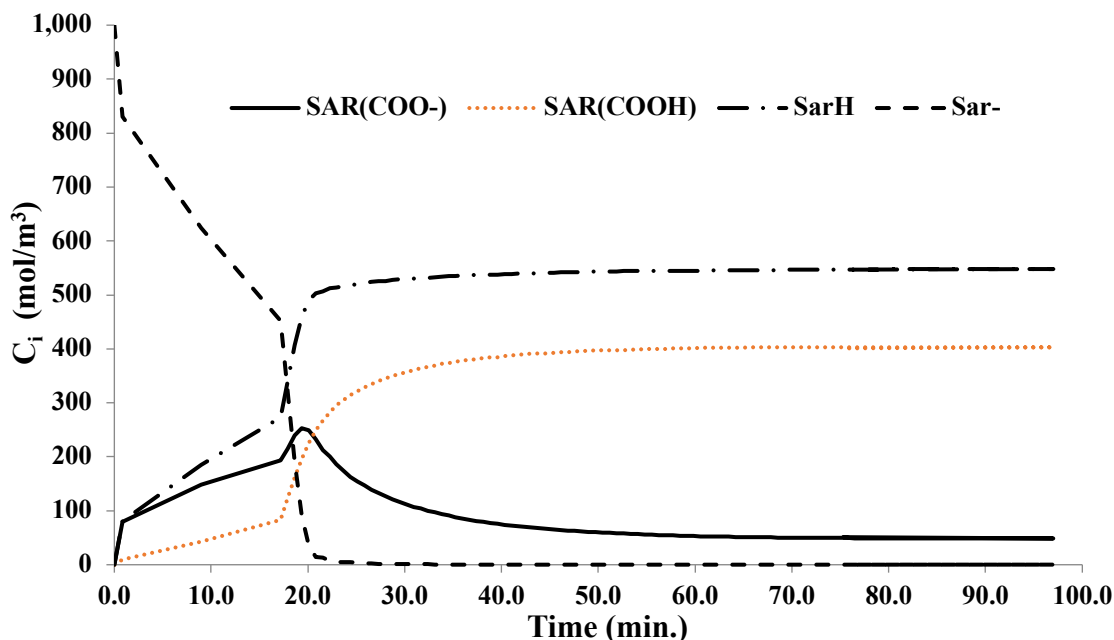


Figure 25. Time variation of all amino acid chemical species.

The results presented in Figure 25 show that there is a sharp decrease in the amount of the salt form of the amino acid due to reaction (51). In fact, the decrease in the concentration of the salt form of the amino acid is what produces the breakthrough curve. After the breakthrough, there is very little amino acid in salt form; practically, all amino acid is in protonated form. Furthermore, the steady-state amount of protonated amino acid is above the stoichiometric 0.5 factor indicated by eq. (51). This fact suggests that some decrease in the salt form of the amino acid is not produced by the reaction with CO_2 . Instead, it is produced by equilibrium displacement in reaction (11). At short times, there is an almost identical production of carbamate and protonated amino acid; however, as time increases, due to pH decrease, the carbamate is transformed into protonated carbamate, and this species becomes the predominant one. In all cases, the summation of all these species is equal to the original amount of amino acid.

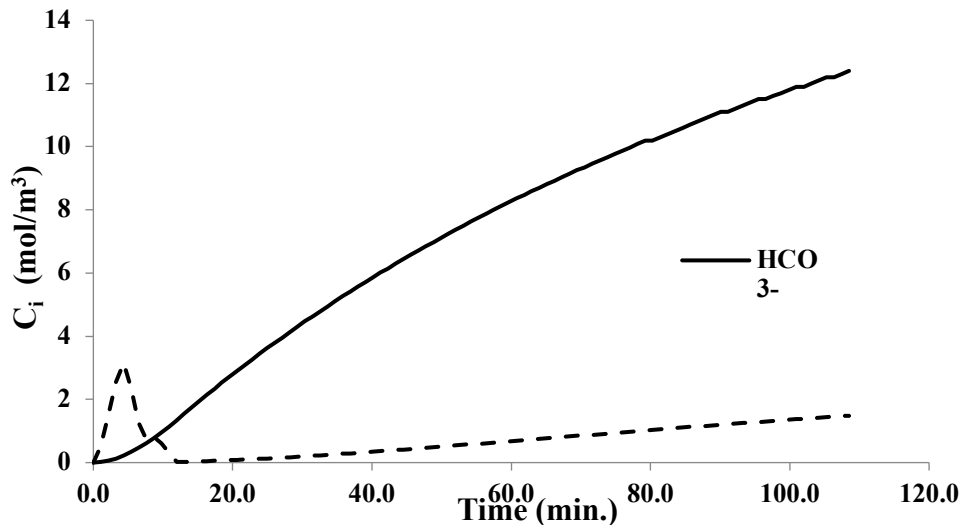


Figure 26. Variation of the bicarbonate and carbonate concentrations with time.

The interaction between the bicarbonate and the carbonate ions is shown in Figure 26. At short times, when the pH is high, the carbonate ion is the predominant chemical species. As time increases and pH decreases, the bicarbonate ion becomes the most important. The concentration of the bicarbonate ion increases continuously throughout the process; however, the absolute value is much lower than the carbamate products of the amino acid reaction. The increase in the bicarbonate ion concentration, at almost constant pH, produces an increase in the carbonate concentration after breakthrough.

Bubble Column Results. A computer code was developed to implement the bubble-column model presented in the theoretical section. Table AII in the appendix contains the kinetic data used in all the calculations. Table AIV in the appendix contains the standard set used in our calculations. Typical results are plotted in Figures 27, 28, 29, and 30. A dimensionless time ($t = \frac{time \ u_1}{H}$) has been used as a second parameter in these Figures.

In Figure 27, we show typical axial concentration profiles of CO_2 in the gas phase. The concentration of CO_2 is highest at the base of the column, $z = 0$, and drops as we approach the top, $z = 1$. The results in Figure 27 show that, as time increases, the axial concentration profile of CO_2 approaches the steady-state value.

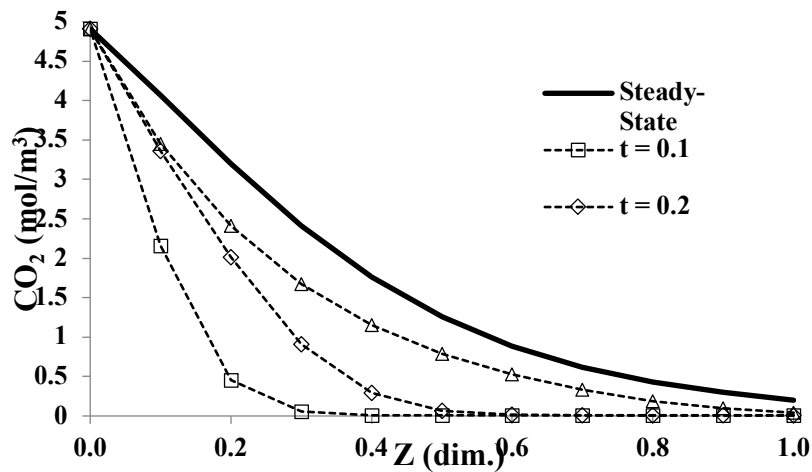


Figure 27. Carbon dioxide axial concentration profile.

The CO₂ concentration in gas phase is associated with the consumed concentration of sarcosine as the amino acid enters from the top and reacts with the CO₂ being transferred from the gas phase. The corresponding amino acid axial profile is shown in Figure 28. This Figure shows that the time evolution of the sarcosine salt axial profile in liquid phase is more complex than the corresponding CO₂ profile in gas phase. The values of the amino acid salt concentration are higher at the top of the column while the reverse is true at the bottom of the column. This behavior is the reverse of the gas phase CO₂ profile. As times increases the concentration of the amino acid ion decreases continuously throughout the column until converging to the steady-state solution.

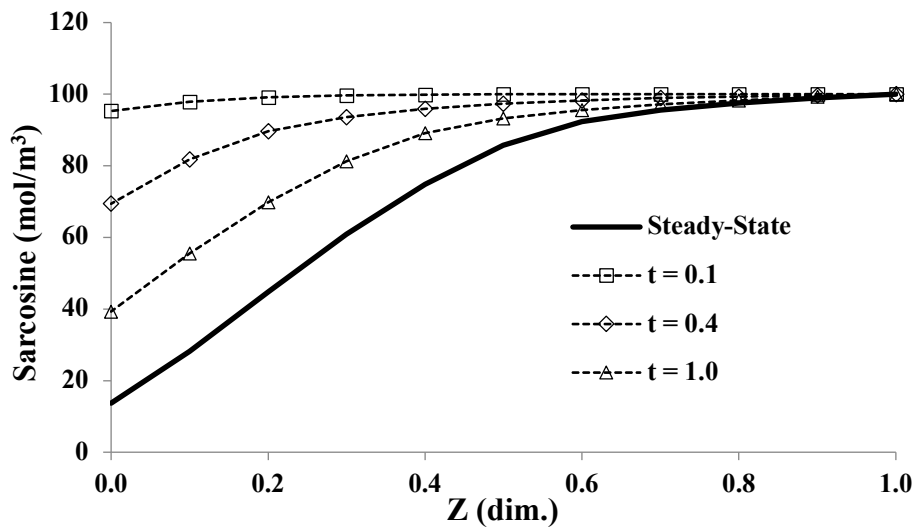


Figure 28. Sarcosine axial concentration profile.

The results shown in Figure 28 also suggest that there is a complex equilibrium among the different amino acids forms, pH, and the products of the reaction of the amino acid salt with CO₂. To further investigate the behavior of this process, we plotted the axial variation of pH at steady-state in Figure 29.

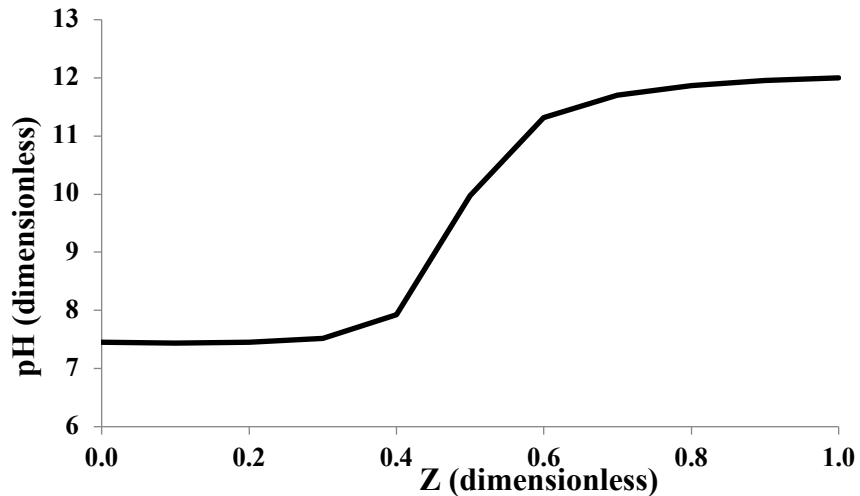


Figure 29. Axial pH variation at steady-state.

The simulation results presented in Figure 29 show that, at steady-state, there is a continuous change in pH throughout the column. The values are high at the top (12.2) while they are almost neutral (7.5) at the bottom.

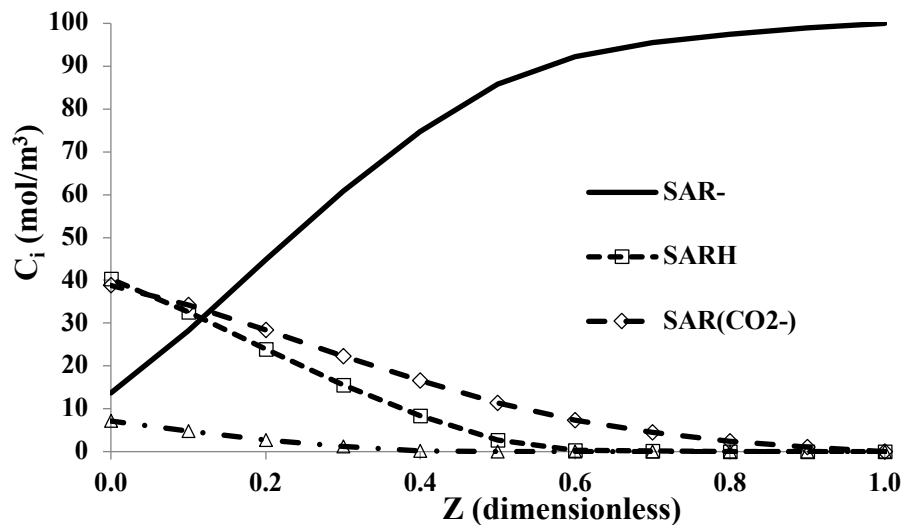


Figure 30. Axial variation of amino acid compounds at steady-state.

We can see in Figure 30 that, in the top half of the column, the concentration of the reaction products is small. The carbamate, SAR(CO₂⁻), and protonated amino acid (SARH) concentrations increase continuously from the top to the bottom of the column. Low pH and increasing CO₂ concentration in the bottom half produce this behavior. The decreasing pH in the bottom half also produces an increasing protonated carbamate, SAR(CO₂H), concentration. At the bottom, $z = 0$, the concentration of both products in reaction (51) approaches the stoichiometric ratio.

Conclusions. A reaction scheme for the reactive CO₂ absorption by amino acids has been proposed. Two reactor models, for a two-phase batch reactor and a bubble column, based upon

transient mass and energy balances for several different chemical species commonly present in CO₂ gas-liquid absorption have been developed. Computer codes have been written to implement the proposed models. Simulation results for both reactor models have been obtained. The complex interaction among pH, amino acid forms, and different reaction products has been investigated. In the two-phase batch reactor, breakthrough of carbon dioxide in the gas phase has been observed. The breakthrough behavior is produced by significant amino acid consumption at short times. We also observed in both reactors a significant decrease in the pH value with time. The bubble column model allows calculation of the axial profiles of the different chemical compounds. The CO₂ axial concentration in the gas phase decreases significantly from bottom to top. Consequently, most of the reactions occur in the bottom half of the column. There is also a significant decrease in the pH value at the bottom half of the column. The low pH at the bottom half plus the high CO₂ concentration produces significant reduction in the salt amino acid concentration. In conclusion, the models presented in this work can be useful tools in simulating and controlling the reactive CO₂ absorption processes in various types of reactors.

5. TECHNO-ECONOMIC ANALYSIS

The goal of this analysis was to estimate the economics of the carbon capture technology with amino acid/guanidine and compare with the economics of the MEA benchmark. The premise was that with the amino acid/guanidine system the CO₂ is precipitated out of the liquid phase. Since only the precipitated solid slurry needs to be heated, instead of the bulk solution, the regeneration energy should be smaller than the regeneration energy needed by the MEA system. Figure 31 illustrates the separation scheme for the guanidine system.

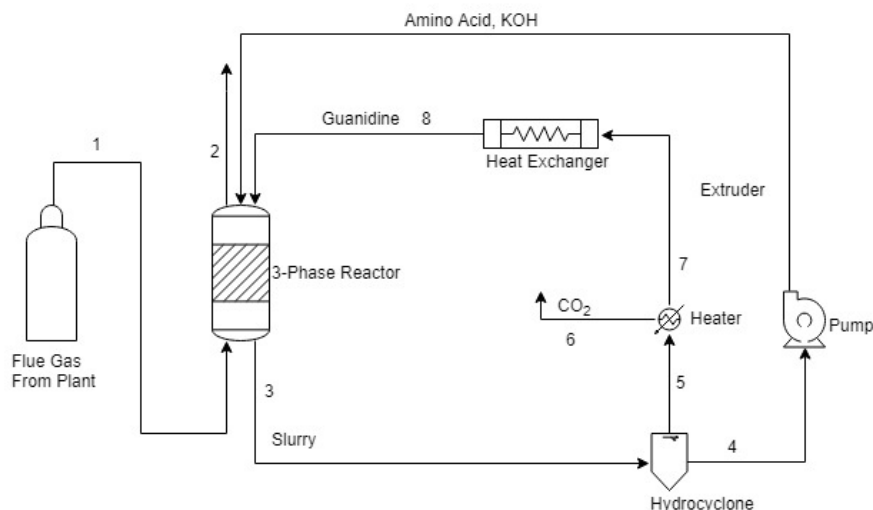


Figure 31. The amino acid/guanidine system for CO₂ capture generates a slurry. Passing through a hydrocyclone, the slurry becomes concentrated before regeneration, and a separated liquid phase is recycled back to the 3-phase absorber without regeneration.

Assumptions. A techno-economic evaluation was conducted on a supercritical black coal fired power plant with a 500MW capacity. The levelized cost of electricity production without carbon capture was assumed to be \$90/kWh. For the purpose of determining solvent flow requirements, it was assumed that the power plant produced 0.808 ton CO₂ per MWh of energy generated. Sorbent losses were estimated at around 2.25 kg solvent per ton CO₂ captured. Both separation

schemes evaluated below were designed to ensure 90% of incoming CO₂ is separated from the flue gas before being purged. The inlet flue gas was characterized as follows: 75% mol N₂, 13% mol CO₂, 7% mol H₂O, 5% mol O₂, 450 ppm NO_x, and 400 ppm SO_x.

5.1 MEA Benchmark Calculations

The economics of the MEA benchmark was evaluated on a 500MW supercritical black coal power plant using the Integrated Environmental Control Model (IECM) developed at Carnegie Mellon University. Figure 32 illustrates the MEA setup used for comparison, while the economics evaluated by IECM are tabulated and presented in Tables 4-7.

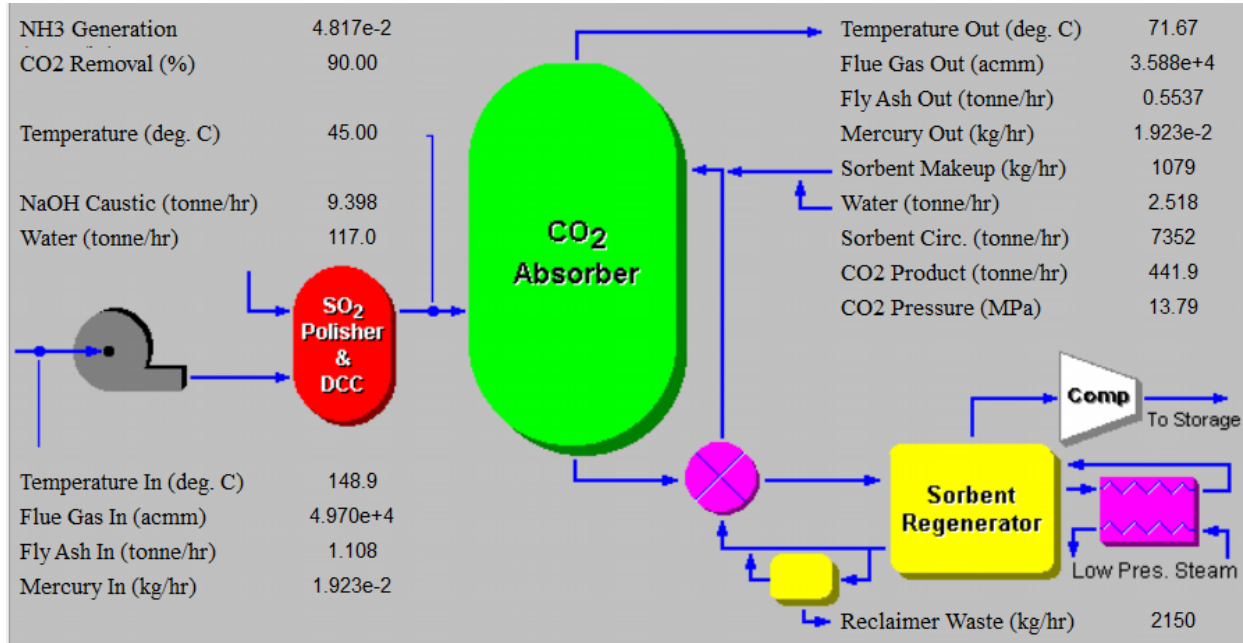


Figure 32. MEA model reaction scheme used as a benchmark for comparison.

Table 4a. Overall Plant Parameters

Important Performance & Cost Factors	Value
Net Electrical Output (MW)	397.200
Annual Operating Hours (hours)	6575.000
Annual CO ₂ Removed (ton/hr)	441.800
Flue Gas Fan Use (MW)	15.230
Sorbent Pump Use (MW)	1.127
CO ₂ Compression Use (MW)	52.110
Sorbent Regen. Equip. Energy (MW)	144.500

Table 4b. Overall Plant Parameters (continued)

Costs of CO ₂ Avoided & Captured	Value
Power Plant with CCS	
CO ₂ Emitted (kg/kWh)	0.124
CO ₂ Captured (kg/kWh)	1.113
Cost of Electricity (\$/MWh)	129.040

Reference Plant (Without Carbon Capture)	
CO ₂ Emitted (kg/kWh)	0.808
Cost of Electricity (\$/MWh)	90.000
Plant with Carbon Capture	
Added Cost of Carbon Capture (\$/MWh)	39.040
Cost of CO ₂ Avoided (\$/ton)	56.200
Cost of CO ₂ Captured (\$/ton)	31.790

Table 5. Total Cost of CO₂ Capture

Cost Component	M\$/yr	\$/MWh	CO₂ Separation (\$/ton separated)	Percent Total
Annual Fixed Cost	13.99	5.358	4.817	7.81
Annual Variable Cost	106.80	40.910	33.740	59.60
Total Annual O&M Cost	120.80	46.270	38.560	67.40
Annualized Capital Cost	58.24	22.300	20.020	32.50
Total Levelized Annual Cost	179.10	68.570	58.580	100.00

Table 6a. Operation and Maintenance Costs

Variable Cost Component	Levelized O&M Cost (\$/MWh)	Cost (\$1000)
Sorbent	7.036	18,134
Corrosion Inhibitor	1.407	3,626
Activated Carbon	0.202	519
Caustic (NaOH)	11.880	30,619
Reclaimer Waste Disposal	1.385	3,569
Electricity	15.520	40,001
Water	0.108	277
CO ₂ Storage	3.378	8,706
Total Variable Costs	40.900	105,415

Table 6b. Operation and Maintenance Costs (continued)

Fixed Cost Component	Levelized O&M Cost (\$/MWh)	Cost (\$1000)
Operating Labor	0.302	779
Maintenance Labor	1.774	4,572
Maintenance Material	2.660	6,855
Administrative & Support Labor	0.623	1,604
Total Fixed Costs	5.358	13,809
Total O&M Costs	46.270	119,256

Table 7. Capital Costs

CO₂ Capture Process Area Costs	Capital Cost (\$/kW-net)	Cost (\$1000)
SO ₂ Polisher/Direct Contact Cooler	85.67	\$33,582

Flue Gas Blower	15.09	\$5,915
CO ₂ Absorber Vessel	213.20	\$83,574
Heat Exchangers	17.75	\$6,958
Circulation Pumps	36.56	\$14,331
Sorbent Regenerator	133.90	\$52,488
Reboiler	65.84	\$25,809
Steam Extractor	9.16	\$3,592
Sorbent Reclaimer	19.76	\$7,745
Sorbent Processing	21.61	\$8,471
Drying and Compression Unit	156.50	\$61,348
Process Facilities Capital	775.20	\$310,080

Table 7. Capital Costs (continued)

CO₂ Capture Plant Costs	Capital Cost (\$/kW-net)	Cost (\$1000)
Process Facilities Capital	775.20	303,878
General Facilities Capital	77.52	30,387
Engineering & Home Office Fees	54.25	21,266
Process Contingency Cost	77.52	30,387
Project Contingency Cost	181.40	71,108
Interest Charges (AFUDC)	84.62	33,171
Royalty Fees	3.88	1,519
Preproduction (Startup) Cost	40.01	15,683
Inventory (Working) Capital	5.83	2,284
Financing Cost	0	0
Other Owner's Costs	0	0
Total Capital Requirement (TCR)	1300.00	509,600
Effective TCR	1300.00	509,600

The cost of CO₂ avoided is a metric used to compare the relative cost of removing CO₂. The equation used to calculate the cost of CO₂ avoided is represented by Equation 1.

$$CO_{2\text{ avoided}} = \frac{LCOE_{CCS} - LCOE_{ref}}{\text{Intensity}_{ref} - \text{Intensity}_{CCS}} \quad (1)$$

Here, LCOE is the levelized cost of electricity (\$/MWh), and Intensity is the amount of CO₂ produced per MWh of energy (ton CO₂/MWh). The subscript ‘CCS’ refers to the power plant using carbon capture and the subscript ‘ref’ denotes the reference plant that does not treat the flue gas.

From the IECM model, a value of \$56.20 was determined for the cost per ton of CO₂ avoided. This calculated value is similar to costs calculated in Raksajati et al. (2016).

5.2 Amino Acid/Guanidine System Calculations

In theory, the amino acid/GBIG system should be more efficient than MEA in regeneration since only the slurry containing the guanidine precipitate (not all the liquid solvent) needs to be heated. The amino acid/GBIG reaction scheme will, however, require larger capital costs for the bubble

column absorber and the hydrocyclone, shown in Figure 31, which will be required to separate the slurry. The absorber vessel required for guanidine is expected to be larger than a standard packed bed column used for MEA due to (i) the lower mass-transfer performance of bubble columns compared to that of packed columns and (ii) the reduced mass-transfer driving force because of the recycled stream of CO₂-saturated solvent from the hydrocyclone. Table 8 includes details of the compositions of streams shown in Figure 31.

Table 8. Mass balance for the amino acid/GBIG CO₂ capture scheme (mol/hr)

Stream	From	To	Temperature (°C)	CO ₂ Dissolved	CO ₂	N ₂
1	Flue Gas	Reactor	25	0	9.18E+06	2.59E+07
2	Reactor	Purge	25	0	9.18E+05	2.59E+07
3	Reactor	Hydrocyclone	25	2.33E+07	0	0
4	Hydrocyclone	Reactor	0	1.50E+07	0	0
5	Hydrocyclone	Heater	0	8.26E+06	0	0
6	Heater	Purge	120	0	8.26E+06	0
7	Heater	Heat Exchanger	120	0	0	0
8	Heat Exchanger	Reactor	40	0	0	0

Stream	KOH	Sarcosine	Guanidine	Water	Total
1	0	0	0	0	3.50E+07
2	0	0	0	0	2.68E+07
3	2.50E+07	2.50E+07	6.26E+06	1.37E+09	7.96E+07
4	2.50E+07	2.50E+07	0	1.37E+09	6.51E+07
5	0	0	6.26E+06	0	1.45E+07
6	0	0	0	0	8.26E+06
7	0	0	6.26E+06	0	6.26E+06
8	0	0	6.26E+06	0	6.26E+06

Solvent Regeneration Energy Penalty. The energy penalties for various chemical absorption solvents are presented in Table 9. The penalty is represented in MW_e, which is the power required multiplied by the energy efficiency of coal (assumed to be 40%).

Table 9. Regeneration energy requirements of chemical absorption technologies

Compound	Regeneration Energy (kJ/kg CO ₂)	Total Power Required (MW)	Energy Penalty (MW _e)
Potassium taurate*	3500	392.77	157.11
Taurine promoted K ₂ CO ₃ *	3000	336.66	134.66
MEA*	4400	493.77	197.51
Bis-guanidine	3443	386.38	154.55

*These values were taken from Wiley et al (2016).

Hydrocyclone. A hydrocyclone was used to separate the slurry exiting the bubble column reactor. Initially, a screw extruder and a series of conveyer belts were considered to transport the solid GBIG after regeneration. Correlations found in Seidar et al suggest that using conveyers or screw

extruders would be impractical and expensive since more than 1000 screw extruders or more than 500 conveyer belts would be required to operate simultaneously to transport the guanidine. Transporting the guanidine back into the column would be more efficiently handled if it was transported in the form of a Newtonian slurry. Solid percentages (by weight) up to 40% were evaluated.

5.3 Economic Calculations

The IECM program (Carnegie Mellon University) was used to evaluate the economics of the bis-guanidine setup. Here, the regeneration energy was scaled to include the presence of liquid in the guanidine slurry. Tables 9A-D presented below tabulate important economic parameters calculated by the IECM program.

Table 9A. Economics of 60% by mass solvent in slurry

Technology	Capital Required (M\$)	Capital Required (\$/kW-net)	Revenue Required (M\$/yr)	Revenue Required (\$/MWh)
In-Furnace NO _x Control	7.15	17.90	0.91	0.35
Post-Combustion NO _x Control	29.54	73.98	6.70	2.55
CO ₂ Capture, Transport & Storage	503.50	1261.00	174.20	66.35
Hydrocyclone	0.77	1.93	0.07	0.29
Subtotal	540.95	1354.80	181.88	69.54
Cooling Tower	66.89	167.50	20.67	7.87
Wastewater Control	0.00	0.00	0.00	0.00
Base Plant	822.90	2061.00	126.40	48.15
Land	0.78	1.94	8.75E-02	3.33E-02
Emission Taxes	0.00	0.00	0.00	0.00
Total	1431.52	3585.24	329.03	125.60
Cost of CO ₂ Avoided (\$/ton)				51.26

Table 9B. Economics of 80% by mass solvent in slurry

Technology	Capital Required (M\$)	Capital Required (\$/kW-net)	Revenue Required (M\$/yr)	Revenue Required (\$/MWh)
In-Furnace NO _x Control	7.148	17.95	0.91	0.35
Post-Combustion NO _x Control	29.83	74.90	6.78	2.59
CO ₂ Capture, Transport & Storage	509.90	1280.00	176.60	67.44
Hydrocyclone	0.77	1.93	0.07	0.29
Subtotal	547.64	1374.78	184.35	70.67

Cooling Tower	66.41	166.70	20.58	7.86
Wastewater Control	0.00	0.00	0.00	0.00
Base Plant	829.50	2083.00	127.60	48.72
Land	0.7755	1.947	8.75E-02	3.34E-02
Emission Taxes	0.00	0.00	0.00	0.00
Total	1444.33	3626.42	332.62	127.28
Cost of CO ₂ Avoided (\$/ton)				53.69

Table 9C. Economics of 0% by mass solvent in slurry

Technology	Capital Required (M\$)	Capital Required (\$/kW-net)	Revenue Required (M\$/yr)	Revenue Required (\$/MWh)
In-Furnace NO _x Control	7.148	16.08	0.9133	0.3126
Post-Combustion NO _x Control	29.27	65.86	6.451	2.208
CO ₂ Capture, Transport & Storage	326.8	735.4	143.2	49.00
Hydrocyclone	0.77	1.93	0.07	0.29
Subtotal	483.0	1087	180.4	61.76
Cooling Tower	69.16	155.6	21.09	7.220
Wastewater Control	0.0	0.0	0.0	0.0
Base Plant	805.1	1812	144.2	49.36
Land	0.7755	1.745	8.746e-2	2.994e-2
Emission Taxes	0.0	0.0	0.0	0.0
Total	1358	3056	345.8	118.4
Cost of CO ₂ Avoided (\$/ton)				50.49

Number of conveyers needed: 43

Cost of conveyer: \$3.03E6

Power Rating of Conveyer: 170 HP

Table 9D. Economics of MEA

Technology	Capital Required (M\$)	Capital Required (\$/kW-net)	Revenue Required (M\$/yr)	Revenue Required (\$/MWh)
In-Furnace NO _x Control	7.14	18.00	0.91	0.35

Post-Combustion NO _x Control	30.14	75.87	6.85	2.63
CO ₂ Capture, Transport & Storage	516.40	1300.00	179.10	68.57
Subtotal	553.68	1393.87	186.86	71.54
Cooling Tower	65.91	165.90	20.49	7.84
Wastewater Control	0.00	0.00	0.00	0.00
Base Plant	836.40	2106.00	128.80	49.32
Land	0.77	1.95	8.75E-02	3.35E-02
Emission Taxes	0.00	0.00	0.00	0.00
Total	1456.77	3667.72	336.24	128.74
Cost of CO ₂ Avoided (\$/ton)				56.20

Thus, from the values presented in the tables above, there is economic potential in carbon capture using amino acid/GBIG slurry. Based on the assumptions made for the analysis, a 10% reduction in the cost of CO₂ avoided is possible.

6. CONCLUSIONS

In this bench-scale study, we demonstrated an effective approach to carbon dioxide separation from flue gas based on CO₂ absorption by aqueous amino acid salts (i.e., potassium glycinate, potassium sarcosinate), followed by amino acid regeneration and bicarbonate removal by crystallization with a simple bis-iminoguanidine base (GBIG). The measured cyclic capacities of 0.2-0.3 mol CO₂/mol amino acid, obtained from multiple absorption/regeneration cycles, are in the same range as the corresponding values reported for aqueous amine sorbents. In the final step, the CO₂ is released in the solid state by mild heating of the GBIG bicarbonate crystals. By adding the additional crystallization step, this hybrid solvent/solid-state approach circumvents the energy-intensive processes of heating and boiling aqueous solutions, typically involved in traditional solvent-based carbon capture methods. This approach results in a significantly lower regeneration energy compared to industrial benchmarks, like aqueous monoethanolamine or sodium glycinate.

The glycine and sarcosine sorbents were tested for CO₂ absorption using a stirred bubble tank reactor and a bubble column reactor. The experimental information thus obtained was used to develop a mathematical model for the prediction of the CO₂ absorption performance under a wide range of operating conditions. A techno-economic analysis was performed to evaluate the economic feasibility of this new CO₂ capture technology and compare it with the MEA benchmark. The analysis found a 10% reduction in the cost of CO₂ avoided compared to MEA.

Finally, another potential advantage of the hybrid glycine/sarcosine + GBIG system is that, by avoiding heating and boiling the amino acid solutions, sorbent loss through evaporation and degradation is minimized. The regeneration process involves heating the solid GBIG alone, and the initial tests indicated very high thermal stability with no decomposition detected after one week of heating the crystals at 120 °C in air. More extensive tests over hundreds of absorption/regeneration cycles at larger scales and under real-world conditions are necessary to fully evaluate this promising new approach to CO₂ separation and develop it into an energy-efficient and cost-effective carbon capture technology.

7. REFERENCES

- 1) Akita, K. and Yoshida, F. "Bubble Size, Interfacial Area, and Liquid-Phase Mass Transfer Coefficient in Bubble Columns," *Ind. Eng. Chem. Process Des. Dev.*, **13**, 84–91, 1974.
- 2) Benamor, A., et al. "Reaction Kinetics of Carbon Dioxide in Aqueous Blends of N-methyl-diethanolamine and Glycine using the Stopped Flow Technique," *J. Nat. Gas Sci. Eng.*, **33**, 186–195, 2016.
- 3) Brethomé, F. M., Williams, N. J., Seip, Ch. A., Kidder, M., and Custelcean, R., "Direct Air Capture of CO₂ via Aqueous-Phase Absorption and Crystalline-Phase Release using Concentrated Solar Power," *Nature Energy*, **3**, 553-559, 2018.
- 4) Bosch, H., Versteeg, G. F., and van Swaaij, W. P. M. "Gas-Liquid Mass Transfer with Parallel Reversible Reactions-III. Absorption of CO₂ into Solutions of Blends of Amines." *Chem. Eng. Sci.*, **44**, 2745-2750, 1989.
- 5) Bouaifi, M., Hebrard, G., Bastoul, D., and Roustan, M. "A Comparative Study of Gas Hold-Up, Bubble Size, Interfacial Area and Mass Transfer Coefficients in Stirred Gas-Liquid Reactors and Bubble Columns," *Chem. Eng. and Process.*, **40**, 97-111, 2001.
- 6) Chatterjee, S., et al. "Adsorption of Carbon Dioxide on Naturally Occurring solid Amino Acids," *J. Environ. Chem. Eng.*, **4**, 3170–3176, 2016.
- 7) Caplow, M. "Kinetics of Carbamate Formation and Breakdown." *J. Am. Chem. Soc.*, **90**, 6795-6803, 1968.
- 8) Richardson, J. H., Harker, J. H., and Backhurst, J. R. "Chemical Engineering. Vol. 2, Particle Technology and Separation Processes." Oxford; Burlington: Butterworth-Heinemann, publishers, 5th edition, 2008.
- 9) Danckwerts, P. V. "The Reactions of CO₂ with Ethanolamines." *Chem. Eng. Sci.*, **34**, 443-446, 1979.
- 10) Feron, P. H. M. (Ed). Absorption-Based Post-Combustion Capture of Carbon Dioxide. Woodhead Publishing Series in Energy: Number 101, **2016**.
- 11) Gabitto, J. and Tsouris, C. "Carbon Dioxide Absorption Modeling for Off-Gas Treatment in the Nuclear Fuel Cycle." *Int. Journal of Chem. Eng.*, vol. **2018**, ID: 3158147, 2018. <https://doi.org/10.1155/2018/3158147>.
- 12) Gottlicher, G. The Energetics of Carbon Dioxide Capture in Power Plants. U.S. Department of Energy, Office of Fossil Energy, NETL, **2004**.
- 13) Greer, T., Bedelbayev, A., Igreja, J. M., Pereira Gomes, J. F., and Lie, B. "A Dynamic Model for the De-Absorption of Carbon Dioxide from Monoethanolamine Solution," *Proceedings SIMS 2008*, Oslo University College, October 7-8, 2008.
- 14) Greer, T., "Modeling and Simulation of Post Combustion CO₂ Capturing," *Ms. Thesis*, Telemark University College, Faculty of Technology, 2008.
- 15) Hagewiesche, D. P., Ashour, S. S., Al-Ghawas, H. A., and Sandall, O. C. "Absorption of Carbon Dioxide into Aqueous Blends of Monoethanolamine and Methyl-diethanolamine," *Chem. Eng. Sci.*, **50**, 1071-1079, 1995.
- 16) Hikita, H. and Kikukawa, H. "Liquid-phase Mixing in Bubble Columns: Effect of Liquid Properties," *Chem. Eng. J.*, **8**, 191–197, 1974.
- 17) International Energy Agency (2016). 20 Years of Carbon Capture and Storage. www.iea.org/publications/freepublications/publication/20YearsofCarbonCaptureandStorage_WEB.pdf.
- 18) Jockenhövel, T. and Schneider, R. "Towards Commercial Application of a Second Generation Post-Combustion Capture Technology—Pilot Plant Validation of the Siemens Capture Process and Implementation of a First Demonstration case," *Energy Procedia*, **4**, 1451–1458, 2011.

- 19) Jockenhövel, T., Schneider, R., and Rode, H. "Development of an Economic Post-Combustion Carbon Capture Process," *Energy Procedia*, **1**, 1043–1050, 2009.
- 20) Kasturi, A. S., et al. "Study of Carbon Dioxide Absorption by Amino Acids in Bubble Columns," submitted for this special issue, 2018.
- 21) Kumar, P. S., et al. "Equilibrium Solubility of CO₂ in Aqueous Potassium Taurate Solutions: Part 1. Crystallization in Carbon Dioxide Loaded Aqueous Salt Solutions of Amino Acids," *Ind. Eng. Chem. Res.* **42**, 2832–2840, 2003a.
- 22) Kumar, P. S., et al. "Kinetics of the Reaction of CO₂ with Aqueous Potassium Salt of Taurine and Glycine," *AIChE J.*, **49**, 203–213, 2003b.
- 23) Lawal, A., Wang, M., Stephenson, P., and Yeubg, H. "Dynamic modeling of CO₂-absorption for post combustion capture in coal-fired power plants," *Fuel*, **88** (12), 2455-2462, 2009.
- 24) Lee, J. C. and Meyrick, D. L. "Gas-liquid Interfacial Area in Salt Solutions in an Agitated Tank," *Trans. Inst. Eng.*, **48**, T37, 1970.
- 25) Lewis, W. K. and Whitman, W. G., "Principles of Gas Absorption," *Ind. & Eng. Chem.*, **16**, 1215-1220, 1924.
- 26) Luan, D., Zhang, Sh., Wei, X., and Chen, Y.-M. "Study on Mathematical Model to Predict Aerated power Consumption in a Gas-Liquid Stirred Tank," *Results in Phys.*, **7**, 4085-4088, 2017.
- 27) Mahmud, N., Benamor, A., Nasser, M. S., Al-Marri, M. J., Qiblawey, H., and Tontiwachwuthikul, P. "Reaction Kinetics of Carbon Dioxide with Aqueous Solutions of L-Arginine, Gycine & Sarcosine using the Stopped Flow Technique," *Int. Journal of Greenhouse Gas Control*, **63**, 47-58, 2017.
- 28) Morsi, B. I. and Basha, O. M. "Mass Transfer in Multiphase Systems," Chapter 9 in *Mass Transfer - Advancement in Process Modelling*, by Solecki, M., publishers IntechOpen, 2017, <http://dx.doi.org/10.5772/60516>.
- 29) Perry R. H. and Green D. W., *Chemical Engineers Handbook. 7th edition*, McGraw-Hill, New York, 1999.
- 30) Portugal, A. F., Derks, P. W. J., Versteeg, G. F., Magalhães, F. D., and Mendes, A. "Characterization of Potasium Glycinate for Carbon Dioxide Absorption Purposes," *Chem. Eng. Sci.*, **62**, 6534-6547, 2007.
- 31) Pinsent, B. R. W., Pearson, L., and Roughton, F. J. W. "The Kinetics of Combination of Carbon Dioxide with Hydroxide Ions." *Journal of the Chemical Society, Faraday Transactions*, **52**, 1512–1520, 1956.
- 32) Raksajati, A.; Ho, M. T.; Wiley, D. E. *Industrial & Engineering Chemistry Research* **2016**, *55* (7), 1980–1994.
- 33) Sakwattanapong, R., Aroonwilas, A., and Veawab, A. "Reaction Rate of CO₂ in Aqueous MEA-AMP Solution: Experiment and Modeling." *Energia Procedia*, **1**, 217-224, 2009.
- 34) Seider, W. D.; Lewin, D. R.; Seader, J. D.; Widagdo, S.; Gani, R.; Ng, K. M. *Product and process design principles: synthesis, analysis, and evaluation*; Wiley: Hoboken, NJ, 2017.
- 35) Shen, S., et al. "Kinetics of CO₂ Absorption into Aqueous Basic Amino Acid Salt: Potassium Salt of Lysine Solution," *Environ. Sci. Technol.*, **50**, 2054–2063, 2016.
- 36) Shah, M, Kiss, A. A., Zondervan, E., van der Schaaf, J., and de Haan, A. B. "Gas Holdup, Axial Dispersion, and Mass Transfer Studies in Bubble Columns," *Ind. Eng. Chem. Res.*, **51**, 14268-14278, 2012.
- 37) Shariff, A. M.; Shaikh, M. S. Aqueous Amino Acid Salts and Their Blends as Efficient Absorbents for CO₂ Capture, in *Energy Efficient Solvents for CO₂ Capture by Gas-Liquid Absorption* (Budzianowski, W. M. Editor). Springer, **2016**, 117-151.

- 38) Simons, K., Brilman, D. W. F., Mengers, H., Nijmeijer, K., and Wessling, M. "Kinetics of CO₂ Absorption in Aqueous Sarcosine Salt Solutions: Influence of Concentration, Temperature, and CO₂ Loading," *Ind. Eng. Chem. Res.*, **49**, 9693-9702, 2010.
- 39) Song, H.-J.; Lee, S.; Park, K.; Lee, J.; Spah, D. C.; Park, J.-W.; Filburn, T. P. Simplified Estimation of Regeneration Energy of 30 wt % Sodium Glycinate Solution for Carbon Dioxide Absorption. *Ind. Eng. Chem. Res.* **2008**, *47*, 9925-9930.
- 40) Tavlarides, L. L., Lin, R.; Nan, Y., Yiaccoumi, S., Tsouris, C., Ladshaw, A., Sharma, K., Gabitto, J., and DePaoli, D. "Sorption Modeling and Verification for Off-Gas Treatment." NEUP, 2015, Web.: doi:10.2172/1179788. Download from: <https://neup.inl.gov/>.
- 41) Tsouris, C.; Tavlarides, L.L. " Mass-Transfer Effects on Droplet Phenomena and Extraction Column Hydrodynamics Revisited," *Chem. Eng. Sci.*, **48**, 1503-1515, 1993.
- 42) Vaidya, P. D., et al. "Kinetics of Carbon Dioxide Removal by Aqueous Alkaline Amino Acid salts," *Ind. Eng. Chem. Res.*, **49** (21), 11067–11072, 2010.
- 43) van Krevelen, D. W. and Hoftijzer, P. J., "Kinetics of Gas-Liquid Reactions Part I. General Theory," *Recl. Trav. Chim. Pays-Bas*, **67**, 563-586, 1948.
- 44) van Holst, J., et al. "Kinetic Study of CO₂ with Various Amino Acid Salts in Aqueous Solution," *Chem. Eng. Sci.*, **64**, 59–68, 2009.
- 45) Versteeg, G. F. and van Swaaij, W. P. M. "On the Kinetics between CO₂ and Alkanolamines both in Aqueous and Non-Aqueous Solutions- I. Primary and Secondary Amines." *Chem. Eng. Sci.*, **43**, 573-585, 1988.
- 46) Versteeg, G. F., Holst, J. V., Politiek, P. P, and Niederer, J. P. "CO₂ Capture from Flue Gas using Amino Acid Salt Solutions," [Online] June 2006 available from <http://www.co2-cato.nl/doc.php?lid=317> accessed [9/04/2018].
- 47) Wilkinson, P. M., Haringa, H., and Van Dierendonck, L. L. "Mass Transfer and Bubble Size in a Bubble Column under Pressure," *Chem. Eng. Sci.*, **49**, 1417-1427. 1994.
- 48) Williams, N. J.; Seipp, C. A.; Brethomé, F. M.; Ma, Y.-Z.; Ivanov, A. S.; Bryantsev, V.; Kidder, M. K.; Martin, H. J.; Holguin, E.; Garrabrant, K. A.; Custelcean, R. CO₂ Capture via Crystalline Hydrogen-Bonded Bicarbonate Dimers. *Chem* **2019**, <https://doi.org/10.1016/j.chempr.2018.12.025>.
- 49) Xiang, Q., Fang, M., Yu, H., and Maeder, M. "Kinetics of the Reversible Reaction of CO₂ (aq) and HCO₃⁻ with Sarcosine Salt in Aqueous Solution," *J. of Phys. Chem. A*, **116**, 10276-10284, 2012.

8. PRODUCTS

8.1 Publications and presentations

This project resulted in 2 conference presentations and 3 manuscripts submitted for publication:

Abishek Kasturi, Austin Ladshaw, Sotira Yiacoumi, Jorge Gabitto, Kathleen Garrabrant, Neil Williams, Radu Custelcean, Costas Tsouris, *CO₂ Absorption from Simulated Flue Gas in a Bubble Column*, presented at the 20th Symposium on Separation Science & Technology for Energy Applications, Gatlinburg, TN, October 22, 2018.

Kathleen Garrabrant, Neil Williams, Erick Holguin, Flavien Brethome, Radu Custelcean, *CO₂ Capture via Absorption with Amino Acids and Guanidine Crystallization*, presented at the 20th Symposium on Separation Science & Technology for Energy Applications, Gatlinburg, TN, October 22, 2018.

J. Gabitto, R. Custelcean, C. Tsouris, *Simulation of Carbon Dioxide Absorption by Amino Acids in Tho-Phase Batch and Bubble Column Reactors*, submitted to *Separation Science and Technology*.

A. Kasturi, A.P. Ladshaw, S. Z. Yiacoumi, J. F. Gabitto, K. A. Garrabrant, R. Custelcean, C. Tsouris, *CO₂ Absorption from Simulated Flue Gas in a Bubble Column*, submitted to *Separation Science and Technology*.

K. A. Garrabrant, N. J. Williams, E. Holguin, F. M. Brethome, C. Tsouris, R. Custelcean, *Energy-Efficient CO₂ Capture from Flue Gas by Absorption with Amino Acids and Crystallization with a Bis-Iminoguanidine*, submitted to *Industrial & Engineering Chemistry Research*.

8.2 Technology commercialization

A CRADA application (NFE-18-07373) with RTM (Germany) for Direct Air Capture of CO₂ via amino acid/bis-iminoguanidine systems has been approved by DOE. The goal of this CRADA is to develop an energy-efficient and cost-effective technology for CO₂ capture from ambient air, and scale it up to pilot scale and eventually to industrial scale.

9. APPENDIX:

Reactions

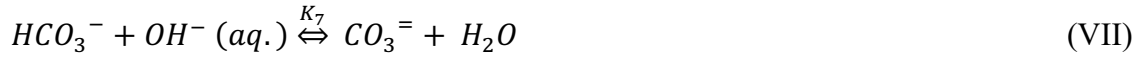
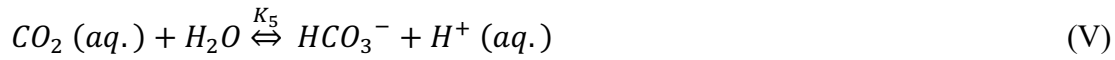
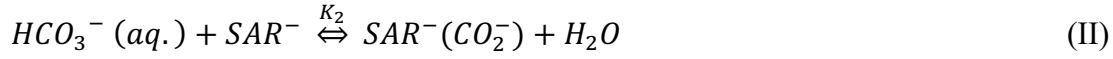
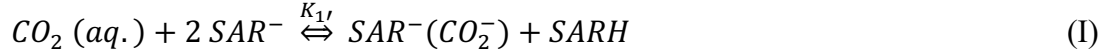


Table AI summarizes all the chemical compounds participating in reactions (I) to (VIII).

Table AI. List of compounds participating in the reaction scheme.

Compound N°	Gas	Liquid
1	N ₂ (g)	SAR ⁻
2	O ₂ (g)	SAR ⁻ (CO ₂ ⁻)
3	CO ₂ (g)	SAR ⁻ (CO ₂ H)
4	H ₂ O (g)	CO ₂ (aq.)
5	----	H ₂ O
6	----	HCO ₃ ⁻
7	----	OH ⁻
8	----	H ⁺
9	----	CO ₃ ⁼

10	----	SARH
11	----	N ₂ (aq.)
12	----	O ₂ (aq.)

Kinetic Data

Table AII. Information used in solving the proposed reaction model.

Eq. No Reaction	Forward Rate (k_{fi})	Equilibrium Constant	Reverse Rate (k_{ri})
I (51)	$k_{1f} = 8.3E8 (M^{-1}s^{-1})$ $Exp(-3127/T_1)$	$K_1 = k_{1f} / k_{1r}$	$k_{1r} = 4E13(s^{-1})$ $Exp(8004/T_1)$
II (5)	$k_{2f} = 3.59E5(mM^{-1}s^{-1})$ $Exp(-7400/T_1)$	$K_2 = k_{2f} / k_{2r}$	$k_{2r} = 4931.6 (mM^{-1} s^{-1})$ $Exp(-8004/T_1)$ (Ref. 1)
III (6)	$k_{3f} = 4.52E7 (M^{-1} s^{-1})$ $*10^{(-909.1/T_1)}$	$K_3 = 4.52E10 (M^{-1}) *10^{(-909.1/T_1)}$	$k_{3r} = 1.E-3 (s^{-1})$
IV (7)	$k_{4f} = 1.88E12*$ $Exp[-7698./T_1]$	$K_4 = k_{4f}/k_{4r} =$ (Ref. 15)	$k_{4r} = 2.491E16*Exp[-1.367E4/T_1]$
V (8)	$k_{5f} = 4.32E-7$	$K_5 = 10^{(3404.71/T_1 + 0.032786*T_1 - 14.8435)}$	$K_{5r} = (k_{5f})/K_6$
VI (9)	$k_{6f} = 3.6E-10$ $(s^{-1} mM^{-1})$	$K_6 = 1.58E-3 (mM)*Exp(-6832/T_1)$	$k_{6r} = (k_{6f})/K_6$
VII (10)	$k_{7f} = 1.E3$	$K_7 = 4.474e-3(mM)*Exp(5325/T)$	$k_{7r} = (k_{7f})/K_7$
VIII (11)	$k_{8f} = 0.1$	$K_8 = 2.83E-5*Exp(6832/T)$	$k_{8r} = (k_{8f})/K_8$

Table AII summarizes all the rate equations used in the model. The first number in the first column is the equation number used in the Appendix. The second number refers to the original equation number used in the article.

Simulation Parameters

Table AIII. Typical set of values used in the simulation of the two-phase batch reactor.

Parameter	Units	Default value	Range
Reactor Volume (V_l)	m^3	1.0E-3	0.5E-3 – 2.E-3
Blade Height (b_i)	m	0.02	0.01 – 0.04
Impeller diameter (d_i)	m	0.05	0.01 – 0.1
Tank diameter (d_T)	m	0.10	0.05 – 0.20
Gas flow rate (Q_g)	m^3/s	6.67E-5	1.67E-5 – 16.70E-5
Input CO ₂ molar fraction (x_{CO_2})	-	0.12	0.02 – 0.2
Initial pH	-	12	10 – 14
Rotational speed (N)	1/s	6.67	1.67 – 11.67

Table AIV. Typical set of values used in the simulation of the bubble column.

Parameter	Units	Default value	Range
Height (H)	m	1	0.5 – 2
Tower diameter (d_c)	m	0.075	0.025 – 0.25
Input CO ₂ molar fraction (x_{CO_2})	-	0.12	0.02 – 0.20
Liquid phase flow rate (Q_l)	m/s	0.017	0.005 – 0.20
Gas phase flow rate (Q_g)	m/s	0.068	0.02 – 0.80
Input temperature (T)	(K)	298	293 – 313
Sarcosine input concentration (C_{SAR})	(mol/m ³)	100	100 – 1000